UNIVERSIDADE DE LISBOA
FACULDADE DE CIÊNCIAS
DEPARTAMENTO DE ENGENHARIA GEOGRÁFICA, GEOFÍSICA E ENERGIA

Transport Variability of the Canary Current

Teresa Maria Grazina do Carmo Costa

Dissertação

Mestrado em Ciências Geofísicas

Especialização em Oceanografia

2014

UNIVERSIDADE DE LISBOA

FACULDADE DE CIÊNCIAS

DEPARTAMENTO DE ENGENHARIA GEOGRÁFICA, GEOFÍSICA E ENERGIA

Transport Variability of the Canary Current

Teresa Maria Grazina do Carmo Costa

Dissertação

Mestrado em Ciências Geofísicas

Especialização em Oceanografia

Orientadores: Prof. Doutor Alonso Hernández-Guerra e Prof. Doutor Joaquim Dias

2014

Abstract

The Canary Current can be divided into a main branch flowing through the Canarian archipelago and a smaller branch flowing between the easternmost Canary Islands and the northwest of Africa. To study the variability of the water volume transport of the Canary Current, CTD and LADCP data of various RAPROCAN cruises were processed, from February 2006 to December 2012. The 18 CTD stations go from 18.5º-15.5ºW at latitude 29º20'N and from that point on until [28º40'N, 13ºW], through the Fuerteventura-Lanzarote strait. The water mass characteristics were derived from the CTD data, as well as the geostrophic velocities, computed through the thermal wind equation. These velocities were then adjusted through the LADCP drawn reference velocities in order to obtain temporal and spatial variability of the volume transport of the Canary Current. We found a clear difference between the variability of the main branch of this current and the branch flowing through the Lanzarote Passage – the Canary Upwelling Current. The transport of the latter current varies throughout the RAPROCAN cruises approximately between [-3.9; 0.3] Sv, where positive values represent northward transport. A seasonal inversion of this flow of both thermocline and intermediate waters was identified. The southward transport of the main branch of the Canary Current fluctuates between [-6.1; -1] Sv, with the strongest transport taking place in August and the weakest in February 2007. Finally, a comparison between the Canary Current and the upper mid-ocean transport variability of the Atlantic Meridional Overturning Circulation was done. It showed an evident correlation between the upper mid-ocean transport and the Canary Upwelling Current.

Canary Current, volume transport and variability, LADCP, UMO.

Resumo

A Corrente das Canárias pode ser dividida num ramo principal que flui através do arquipélago das Canárias e um ramo secundário que flui entre as ilhas mais orientais das Canárias e entre a costa noroeste de África. Para estudar a variabilidade do transporte de volume de água da Corrente das Canárias, os dados CTD e LADCP de vários cruzeiros RAPROCAN foram processados, desde Fevereiro de 2006 a Dezembro de 2012. As 18 estações CTD desses cruzeiros vão de 18.5º-15.5ºW à latitude 29º20'N e desse ponto em diante, até [28º40'N, 13ºW], através do estreito de Fuerteventura-Lanzarote. O ramo secundário da Corrente das Canárias passa entre as ilhas orientais do arquipélago e a Costa noroeste de África (em inglês: Lanzarote Passage - LP). Este ramo foi denominado de Corrente de Afloramento das Canárias (Canary Upwelling Current – CUC (Pelegrí et al., 2006)) e faz também parte do estudo realizado nesta dissertação.

O Giro Subtropical do Atlântico Norte (GSAN) é composto pelas seguintes principais correntes: a Corrente Equatorial Norte a Sul, a Corrente do Golfo no bordo ocidental, a Corrente dos Açores a Norte e a Corrente das Canárias (CC) no bordo oriental. Este giro anticiclónico é induzido, em conjunto com a força de Coriolis, pelo campo dos ventos alíseos em torno de 20ºN de latitude e pelos ventos de oeste ao redor dos 40ºN. Na maior parte da sua extensão o GSAN está em balanço geostrófico, excepto nos bordos ocidental e oriental da bacia oceânica, onde outros processos físicos se tornam progressivamente mais importantes. A corrente do bordo oriental começou a ter um maior interesse para a comunidade científica apenas nas últimas décadas devido ao seu envolvimento na variabilidade da circulação termohalina meridional do Atlântico Norte (do inglês: Meridional Overturning Circulation - MOC).

Sabe-se hoje em dia que a MOC é responsável por regular o clima da Terra pelo transporte e distribuição de calor e massa através dos oceanos. No Atlântico Norte subtropical, a MOC pode ser decomposta da seguinte forma: o transporte da Corrente do Golfo, o transporte da zona central superior do oceano (inglês: upper mid-ocean - UMO), ou seja, o transporte da superfície até aos 1100 m de profundidade no centro da bacia oceânica (Rayner et al., 2011), e o transporte médio meridional de Ekman da tensão zonal do vento do Atlântico Norte subtropical. Pensa-se que a

Corrente das Canárias esteja relacionada com a MOC através do campo local do rotacional do vento, motivo pelo qual se torna muito importante estudar o transporte da CC e a sua variabilidade.

Estudos anteriores mostram que, para as camadas superiores da Corrente das Canárias, o transporte resultante de Setembro de 2003 é de -4.7 ± 0.8 Sv e para a Corrente de Afloramento das Canárias é de 1.1 ± 0.5 Sv. Outros estudos indicam que no Outono o transporte da termoclina é de -4.5 ± 1.2 Sv no caso da CC e de 1.8 ± 0.1 Sv no caso da CUC, embora em 2009 o transporte da CC fosse mais forte e enquanto o da CUC estava mais fraco. No Inverno estes valores são ainda mais baixos, com um transporte de -1.7 ± 1.0 Sv no ramo principal da corrente, e de 0.5 ± 0.2 Sv no ramo secundário. Para o Verão, outros estudos indicam uma Corrente de Afloramento das Canárias mais forte e direccionada para sul: -2.4 ± 0.1 Sv. Num estudo onde foram analisados dados de nove anos no LP, o transporte mais intenso verificou-se no Inverno com -1.3 ± 1.3 Sv, mas esta inversão da CUC nem sempre acontece, por vezes ocorre mais cedo, no Outono.

Após esta breve introdução sobre a circulação na região em estudo, descreve-se agora resumidamente os dados utilizados e a metodologia adoptada neste trabalho.

O Instituto de Oceanografia y Cambio Global (IOCAG) cedeu dados CTD de oito campanhas oceanográficas no âmbito do projecto da Radial Profunda de Canarias - RAPROCAN. Em três dessas oito campanhas também estavam disponíveis dados LADCP. Detalhes sobre cada campanha e sobre o posicionamento das 18 estações analisadas podem ser vistos na tabela 1 e na figura 1 respectivamente. Note-se que as campanhas foram levadas a cabo durante diferentes estações do ano, com excepção da Primavera. Informações sobre os diferentes processamentos de dados LADCP e a qualidade dos mesmos podem ser encontradas no apêndice da dissertação, na página 32.

Desses dados calculou-se o transporte de volume da Corrente das Canárias, ao qual foi retirado o efeito do transporte de Ekman à camada de superfície da coluna de água. Comparou-se este transporte com o transporte de Sverdrup local para melhor compreender os processos que ditam a variabilidade da CC. Os dados de vento para estes cálculos são provenientes do National Center for Environmental Prediction (NCEP) e interpolados com o modelo de Weather Research and Forecasting (WRF).

Após o ajuste do transporte geostrófico pela informação dos dados de velocidade de LADCP, chegou-se à conclusão que era necessário estabelecer um novo nível de referência para o cálculo da velocidade geostrófica, apenas para o troço zonal das estações analisadas. Finalmente, comparou-se o transporte geostrófico ajustado obtido após a eleição de um nível de referência mais próximo da realidade com o transporte da zona central superior do oceano Atlântico Norte. Este último é proveniente dos programas de Rapid Climate Change - RAPID & RAPID WATCH.

Para mais detalhes sobre os dados utilizados neste trabalho e as equações utilizadas para estes cálculos, tal como as variáveis intervenientes, veja-se a secção 2 e 3 respectivamente.

Passamos agora à apresentação dos resultados. Analisando os gráficos das figuras 2 e 3 verificamos que as massas de água presentes nesta região são: Água Central do Atlântico Norte (North Atlantic Central Water - NACW), Água Intermédia Antárctica (Antarctic Intermediate Water - AAIW), Água Mediterrânica (Mediterranean Water - MW) e Água Profunda do Atlântico Norte (North Atlantic Deep Water - NADW). Os dois últimos tipos não foram encontrados nas estações de 1-5, entre o arquipélago e a costa africana, como se pode constatar com facilidade pelos diagramas Θ-S. Na campanha RAPROCAN 1010 é possível ver indícios de um vórtice mediterrânico (do inglês, mediterranean eddy - Meddy) entre as estações 6-10, imediatamente a oeste das ilhas Lanzarote e Fuerteventura.

A figura 4 mostra a velocidade geostrófica, para cada uma das campanhas RAPROCAN. Aqui nota-se com clareza o nível de referência escolhido a aproximadamente 3000 m de profundidade, onde a velocidade da corrente é nula. Nas estações cuja coluna de água não atinge essas profundidades - no LP - é possível reconhecer uma dinâmica distinta do resto do transecto. Nessa zona existem essencialmente duas células de velocidade opostas, uma para norte e outra para

sul. Geralmente, a corrente que flui para norte está sob a corrente que flui para sul, junto à superfície. Esta tendência inverte-se no Inverno ou até antes, no Outono.

Na figura seguinte, vê-se o transporte de volume, por camada, da superfície até ao fundo. A coluna de água foi dividida em 12 camadas, conforme o seu nível de densidade neutra (ver tabela 2). A camada de superfície já conta com a contribuição do transporte de Ekman, de acordo com os valores da tabela 3, que embora pequeno, não pode ser negligenciado na comparação com o transporte de Sverdrup mais adiante. O transporte resultante é negativo, ou seja para sul, com valores mais altos a menores níveis de densidade neutra. A excepção desde último ponto é a campanha de 1212 onde o sinal do transporte junto à superfície não é muito claro. O transporte mais intenso verifica-se em Agosto e em Outubro.

Para completar esta análise, veja-se a figura 6 sobre o transporte acumulado por pares de estações, focando apenas no transporte da termoclina (linha vermelha). Aqui separou-se o transporte a Este de Lanzarote do transporte da restante parte do transecto, para melhor entender a dinâmica individual destes locais. A inversão da Corrente de Afloramento das Canárias também é visível nestes gráficos ao observarmos a linha entre -14º e -13º de longitude. O sinal incerto do mês de Dezembro devido à presença de vórtices (como se pode constatar pelos máximos e mínimos alternados nos gráficos) explica o que já foi mencionado sobre a figura 5. Apesar disso, torna-se claro que o transporte acumulado da CC é sempre para sul.

A secção 4.3 explica em que medida os dados LADCP ajudam a avaliar a velocidade geostrófica e consequentemente o transporte calculado anteriormente. Para tal, compararam-se individualmente os perfis de velocidade geostrófica e de velocidade LADCP. Através da diferença média entre os dois perfis, obtiveram-se velocidades de referência por cada par de estações. Estas serão por sua vez adicionadas à velocidade geostrófica, criando assim perfis de velocidade ajustada. Isto nem sempre é possível realizar, dependendo do ruido presente nos dados LADCP. Houve vários destes casos na campanha de 1211, como se pode ver pela figura 9.

A figura 10 mostra o transporte de volume resultante, por camada, após o ajuste de LADCP. Comparando com a figura 5, nota-se que o transporte muda de sinal, em profundidade, a um nível de densidade neutra mais perto da superfície que na figura 5. Por este motivo podemos declarar que o nível inicial de referência para o cálculo da velocidade geostrófica terá de ser redefinido. No entanto, se compararmos a figura 11 com a sua homóloga de transporte inicial acumulado (fig. 6), podemos constatar as maiores diferenças do transporte inicial estão nos níveis intermédios e profundos. As semelhanças entre os transportes de termoclina permitem assim o estudo da variabilidade do transporte mesmo entre campanhas sem ajustes de LADCP.

Passemos então aos resultados finais. As figuras 12 e 13 são semelhantes à figura 5, ou seja, mostram o transporte de volume resultante por camada. Para as campanhas com dados LADCP mostram-se duas curvas em cores distintas, para o transporte com e sem ajustamento.

A principal diferença entre as figuras 12 e 13 é que a primeira apenas mostra o transporte resultante para as estações de 1-5, junto à costa africana. Nessa figura, na campanha RAPROCAN 1010, vê-se claramente a fase de transição da direcção da CUC. É nessa altura que a corrente se torna instável após o cessamento dos fortes ventos alíseos de Verão. Isto permite o afloramento do fluxo subsuperficial para norte, instalando-se assim a inversão da CUC visível nas campanhas de 1211 e 1212. A figura 13 já foi gerada após estabelecer um novo nível de referência para o cálculo da velocidade geostrófica. Também aqui nas primeiras camadas de densidade neutra o transporte atinge maiores valores do que em profundidade. No gráfico de 1212 o sinal do transporte é pouco claro, provavelmente devido à sua baixa magnitude. A diferença entre o transporte com e sem ajuste de LADCP está dentro do erro calculado, representado na figura 11, motivo pelo qual a variabilidade do transporte pode ser analisada sem o ajuste de LADCP.

Finalmente temos na figura 14 o transporte acumulado, por par de estações, obtido com o novo nível de referência. O transporte local de Sverdrup está representado pela linha negra, enquanto a laranja podemos ver o transporte acumulado longitudinalmente, composto pelas camadas com transporte resultante para sul (ver figura anterior). Esta linha representa o transporte do ramo principal da corrente das Canárias com um transporte máximo a 0808, em conformidade com os

ventos alíseos fortes neste período. Em 1010 nota-se novamente a presença do Meddy pelo pico abrupto para sul, característico de uma rotação anticiclónica. O transporte de Sverdrup é bastante similar à linha laranja, com a clara excepção de 0902. Este facto será discutido em seguida na secção 5.

O transporte de Sverdrup depende principalmente do rotacional da tensão do vento. Para a região em causa, a distribuição espacial do rotacional apresenta uma estrutura complexa com células alternadamente positivas e negativas a su-sudoeste das ilhas (vide figura 15). Comparando as várias campanhas para o mês de Fevereiro nota-se que existe muita variabilidade, provavelmente devido à passagem de sistemas de baixa pressão que perturbam o campo do vento, próprio desta altura do ano. Apesar disso, é preciso ter em conta que a teoria de Sverdrup foi desenvolvida para o oceano interior, podendo não explicar por completo o transporte de volume na bacia das Canárias. Um resumo da variabilidade dos transportes de volume, de Sverdrup, e de Ekman nessa área pode ser consultado na tabela 5.

Por fim, comparamos a variabilidade do transporte da Corrente das Canárias com a variabilidade da circulação termohalina através da análise do transporte na zona central superior do Atlântico Norte (UMO). Veja-se então na figura 16 o transporte da UMO estandardizado e o correspondente desvio padrão. O transporte estandardizado da Corrente de Afloramento das Canárias varia aproximadamente com a linha da UMO estandardizada, o que se pode ver pelos pontos azuis, vermelhos e amarelos (diferentes modos de calcular a CUC). A excepção é a campanha de 1010 correspondente ao número 6, pois a UMO nesse ano está longe da média (ponto preto). A verde está o transporte estandardizado do ramo principal da CC, apenas para as campanhas com um transporte relativamente substancial. A correlação entre transportes de CC e UMO é muito menor que a correlação com a Corrente de Afloramento das Canárias.

Esta dissertação permitiu estudar a variabilidade do transporte de volume da Corrente das Canárias através do processamento de dados de 8 diferentes campanhas oceanográficas RAPROCAN.

O campo do rotacional da tensão do vento apresenta uma estrutura muito complexa pelo que o cálculo do transporte local de Sverdrup requer algum cuidado nesta região, o que explica, em parte, a discrepância entre os transportes na campanha de 0209.

Identificámos a dinâmica local da Corrente de Afloramento das Canárias, entre o arquipélago e a costa africana. O transporte da CUC varia entre [-3.9; 0.3] Sv, sofrendo uma inversão no fim de Outubro até Dezembro inclusive. O ramo principal da CC varia entre [-6.1; -1] Sv, onde a magnitude máxima é atingida na campanha de 0808 e a mínima em 0207, o que está aproximadamente de acordo com outros estudos referidos na secção 6.

Os resultados confirmam a relação entre as variabilidades mensais do transporte da Corrente de Afloramento das Canárias e do transporte da zona central superior do Atlântico Norte.

Apesar da informação reunida neste trabalho, conclui-se que são necessários mais dados para entender o que está na origem da relação entre a UMO e os ramos da Corrente das Canárias para de futuro ser possível fazer previsões do comportamento da circulação termohalina e o consequente impacto no nosso clima.

Corrente das Canárias, transporte de volume e variabilidade, LADCP, UMO.

Index

1. Introduction

The North Atlantic subtropical gyre (NASG) is a dynamic structure of ocean currents, ranging from 20º-40ºN & from the African coast to approximately 75ºW (Apel, 1999). It is driven by the wind field of westerlies around 40ºN and the trade winds about 20ºN which, with the Coriolis force, induce an anticyclonic rotation to the gyre (Marshall & Plumb, 2008). The four main currents composing the NASG are the North Equatorial Current, the Gulf Stream (GS), the Azores Current and the Canary Current (CC).

The NASG can be divided into a western boundary associated to the GS, an ocean interior and an eastern boundary associated to the CC. The geostrophic balance does apply for most of the NASG, except in the boundaries where other physical processes become progressively more important, when closing in to the continental platform. Consequently, the boundary currents and its physics were the focus of many studies throughout the years such as Munk (1950), Ekman (1923) and Stommel (1948), according to Marshall & Plumb (2008) and Pedlosky (1996), with scientist trying to find models to better describe these individual ocean currents. The Eastern Boundary Currents (EBC) were believed to be of less significance compared to the strong GS flow. Only more recently has the Atlantic's EBC gained attention regarding its role in the Atlantic's Meridional Overturning Circulation's (MOC) variability (Comas-Rodríguez, 2011).

The MOC, also known as the thermohaline circulation or the conveyor belt, is responsible for the heat and mass distribution in the world's oceans and, consequently, for regulating the Earth's climate (Atkinson, 2011) (Comas-Rodríguez, 2011). Warmer water is carried poleward, where it eventually sinks into deep-water layers in the northern North Atlantic. In this process, heat is released to the atmosphere at these latitudes, hence strongly influencing the European weather (Köhl & Stammer, 2008) (Matei et al., 2012). According to Rayner et al. (2011), the MOC can be decomposed into three main components: the Gulf Stream transport, usually measured through the Florida Straits, the upper-mid ocean (UMO) transport between the Bahamas and the African coast and the zonally averaged Ekman transport across the Atlantic. The Atlantic MOC seasonality is dominated by the respective UMO signal, which in its turn depends on Eastern Boundary Current's density variations (Matei et al., 2012). McCarthy et al. (2012) found that when the UMO is stronger-than-average, the NASG circulation is intensified and a reduction of heat transport takes place.

This is not yet fully understood, but the Canary Current variability seems to be related to the Meridional Overturning Circulation (Fraile-Nuez et al., 2010) through the local wind stress curl (Rayner et al., 2011). Therefore, scientists have developed an increasing interest on these currents in order to improve our understanding on the Earth's self-regulating climate mechanism. Only then can we establish how the MOC would respond to CO_2 forcing and how quickly it would respond to the anthropogenic forcing and thus change climate as we know it.

Our contribution was to analyze the transport variability of the NASG's eastern boundary current, the CC, through Conductivity-Temperature-Depth (CTD) & Lowered Acoustic Doppler Current Profiler (LADCP) data. Previous studies assessed the Canary Basin's dynamics in many different ways: through CTD, moorings (Machín et al., 2010), current profilers (Comas-Rodríguez, 2011) as well as satellite imagery (Fraile-Nuez & Hernández-Guerra, 2006). Studies' focuses include eddy characterization around the Archipelago (Pacheco & Hernández-Guerra, 1999), upwelling mechanism in this region (Pelegrí et al., 2005), (Hernández-Guerra et al., 2002), mass and heat transport monitoring, among other fields in oceanographic research.

Hernández-Guerra et al. (2005), Machín et al. (2006), Fraile-Nuez et al. (2010) and Pérez-Hernández et al. (2013) were some of the latest studies that contributed to the transport characterization of the Canary Current. The CC has a main branch that flows through the archipelago and a smaller one that flows through what is known as the Lanzarote Passage (LP), between the Canary Islands and the African continent. The latter one was named by

Pelegrí et al. (2006) as the Canary Upwelling Current (CUC), since it originates from the barotropic and high inertial contribution of the coastal upwelling jet. The inertia explains why the CUC is not an intermittent structure, even when ideal upwelling conditions fade away. We will adopt this term and will apply it throughout this study.

Hernández-Guerra et al. (2005)'s results state that the net thermocline transport in September 2003 is southward (-4.7 ± 0.8 Sv), with a local positive transport of 1.1 ± 0.5 Sv in the LP. The inverse box model of Pérez-Hernández et al. (2013) showed similar results for fall of 2009 with a net negative thermocline transport of -6.2 ± 0.6 Sv and a positive transport of 0.5 ± 0.1 Sv for the CUC. The other two studies have results for all four seasons, although Fraile-Nuez et al. (2010) only concentrates on LP waters. Machín et al. (2006)'s results are in agreement with the first two described works, with strongest thermocline transport in fall (-4.5 ± 1.2 Sv) and a minimum in winter (-1.7 ± 1.0 Sv). In the fall & winter months the LP system behaved different from the rest of the region. The thermocline transport was poleward with a magnitude of 1.8 ± 0.1 Sv & 0.5 ± 0.2 Sv, respectively, as opposed to the strong, negative transport of -2.4 ± 0.1 Sv present in summer. The Fraile-Nuez et al. (2010)'s results for the LP are somewhat different due to the fact that his signal is smoothed through interannual 9 year variability. The transport seems to be low-pass filtered, with smaller values for every season. Furthermore, he found the inversion of the CUC did not occur in every year and when it did, it was in fall, when the strongest southward thermocline transport of -1.3 ± 1.3 Sv took place. Nevertheless, Fraile-Nuez et al. (2010)'s results have associated uncertainties given the fact that they come from mooring measurements. This comes to emphasize the need of other sampling techniques as the LADCP technology applied in some of the RAPROCAN cruises and analyzed in this work.

The next section describes the data analyzed throughout this paper, followed by the corresponding methodology description in section 3. In the fourth section we present the results of this study, and its discussion can be seen in section 5. Section 6 holds the conclusions of this research work.

2. Data

An assembly of oceanographic cruises were carried out in the Canary Basin under the Radial PROfunda de CANarias (RAPROCAN) project. Data from eight of these RAPROCAN cruises was granted by the Instituto de Oceanografía y Cambio Global (IOCAG). All cruises were done on board of the Cornide de Saavedra vessel, except Rap 7 which was executed on the vessel Ángeles Alvariño. Table 1 summarizes the settings of the different cruises, with a simple numbering in the first column, followed by the names of cruises in the second column, the respective period at sea in the third column, the total number of sampled stations of the cruise in the fourth column and the last one describes which of the cruises has LADCP data available.

Table 1 –RAPROCAN cruises and their respective specifications: numbering, cruise name, cruising period, total number of hydrographic stations and availability of LADCP data.

#	Cruises	Dates	Number of total stations	LADCP
1	RAPROCAN 0206	23 Feb.-5 Mar. 2006	21 (radial)	
2	RAPROCAN 0906	6-16 Sep. 2006	28 (radial)	
3	RAPROCAN 0207	16-21 Feb. 2007	28 (radial)	
4	RAPROCAN 0808	20-29 Aug. 2008	27 (radial)	
5	RAPROCAN 0209	20-28 Feb. 2009	27 (radial)	YES
6	RAPROCAN 1010	26-31 Oct. 2010	28 (radial)	
7	RAPROCAN 1211	1-7 Dec. 2011	24 (radial)	YES
8	RAPROCAN 1212	11-17 Dec. 2012	26 (radial)	YES

We chose the first 18 stations that range from 18.5º-15.5ºW at latitude 29º20'N and from that point on until [28º40'N, 13ºW], through the Fuerteventura-Lanzarote strait. Regardless of the campaign year, the stations have the same coordinates and were chosen this way to focus only on the Canary Current (see positioning in map of figure 1). These 8 cruises sampled

Conductivity-Temperature-Depth (CTD) data in three different seasons: summer, autumn and winter. From these seasons, only some of the winter cruises have Lowered Acoustic Doppler Current Profiler (LADCP) data available.

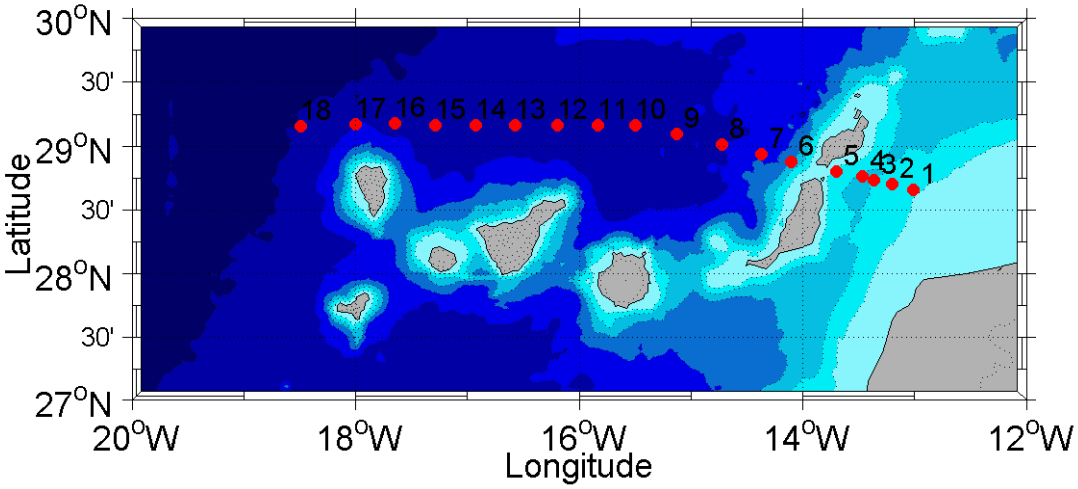

Fig. 1 – Mapping of processed stations of the RAPROCAN cruises. In blue is the ocean bathymetry represented. Isobaths with 750 m spacing, starting at 500 m depth.

After computing geostrophic water transport, the wind stress was derived for the surface Ekman Layer (Fraile-Nuez et al., 2010). Wind velocities were retrieved from the National Center for Environmental Prediction (NCEP) and then interpolated to the grid of the Weather Research and Forecasting (WRF) model (courtesy of Cana-Cascallar, L. (2014), IOCAG). This is a mesoscale, numerical model, which allows to simulate data and to forecast weather conditions through a data assimilation system. The NCEP raw data are transformed through the WRF model in order to account to the smaller scaled orography effects and to have a more accurate spatial resolution (Cana-Cascallar, 2014) (WRF, 2014).

We wanted to compare our thermocline transport with the local Sverdrup transport which is obtained through the wind stress curl. WRF data was also used for this calculation.

To validate the wind stress curl results obtained with this model, we also used data from reanalysis ERA-Interim (ECMWF, 2014), although we do not show the results. ERA-Interim is an assimilation data set, combining atmospheric models and past meteorological observations, from the European Center for Medium range Weather Forecasting (ECMWF).

Lastly, we compared the temporal variability of our results to the UMO variability in order to establish if there is a relationship between the Atlantic Meridional Overturning Circulation and the Eastern Boundary Current dynamics. To this purpose we draw data from programmes Rapid Climate Change (RAPID) and RAPID - Will the Atlantic Thermohaline Circulation Halt? (RAPID-WATCH), where the latter is simply the continuation of the other (RAPID, 2014). They compose a decade (2004-2014) of observations of the MOC components, behavior and characteristics.

2.1 CTD

Data was collected from dual sensors and water samples of a 24-bottle Rosette, for each of the campaigns' 18 casts. Calibrations were done in accordance to World Ocean Circulation Experiment (WOCE) standards (RAPROCAN, 2014) for temperature and depth, and with an AUTOSAL 8400B salinometer for conductivity, with slope corrections (Mock, 2011) .
A total of 11 variables are available from CTD sampling, for each cruise and each station. These include latitude λ, longitude φ, temperature T, salinity S, pressure P, the density ρ, potential temperature θ, potential energy U, potential density σ, neutral density γ and dynamic height D. During the cruises, correction were also done to the measurements, where outliers where discarded and careful extrapolations where done to fill the missing values.

2.2 LADCP

LADCP is an acoustic current-meter, its usage has matured over the last decade. It directly measures velocity profiles within the water column. Through it, we can check the actual velocity in the layer of no motion and establish a reference velocity by comparing the LADCP velocity profile and the geostrophic velocity profile as suggested by Comas-Rodríguez (2011). The adjusted geostrophic velocity obtained through this is then used to compute the water transport between two stations, from the surface to the bottom. Water transport cannot be directly calculated from LADCP measured velocities due to the high noise level of the instrument.

Comas-Rodríguez (2010) describes the sampling methodology of this profiling technique. Two profilers where deployed attached to the Rosette. One of them was a free running Quartermaster ADCP, which worked in down-looking mode at 150 kHz. The other LADCP was a 300 kHz workhorse ADCP, with one up-looking unit run in slave mode, and one down-looking master unit. For further details about the LADCP profiling techniques and the respective obtained velocities please consult the appendix on pages 32 and following. The results of a brief statistic study about the LADCP velocities are showed there.

Many campaigns since 2006 have measured current velocities through LADCP. Unfortunately, the quality of these measurements depends on the experience of handling these kind of profilers. For this reason, the data from the first campaigns had to be discarded. Also, due to problems with the battery of the equipment measurements conducted during RAPROCAN 6 had to be also left out. This left us with only 3 campaigns with apt data to process: RAPROCAN 5, RAPROCAN 7 and RAPROCAN 8, but we believe that it is enough to study the transport of the first layers of the water column.

2.3 Wind data

The set-up for both data sets was the same. WRF-transformed and ERA-Interim data had a grid spacing of 0.125º x 0.125º, a spatial domain ranging from [23.875º - 8.125º] W to [24.125 – 35.875º] N and for the same periods of sampling of each RAPROCAN cruise, with a 6h interval. WRF model results usually perform very well at this resolution, with recognizable small scale features being visible. ERA-Interim has some difficulties in correctly describing the complex wind-eddy field around the Canarian Archipelago, but it does have good atmospheric models to forecast wind speeds (Dee et al., 2013).

2.4 RAPID-WATCH MOC data

The MOC transport and its three respective components are available for download ate the RAPID website www.rapid.ac.uk/rapidmoc. Transport was computed according to the methods of Cunningham et al. (2007), in order to maximize the northward water transport of upper waters of the MOC. The mid-ocean transport is usually defined as the integrated transport from the surface to the depth around 1100 m. Time series have a 12 h step and range from the 2nd April 2004 to 2nd October 2014. The data, in Sverdrup, are low-pass filtered.

3. Methodology

The interactive platform MATrix LABoratory (MATLAB), founded in 1984, is a broadly used tool for numerical programming and visualization (MathWorks, 2014). In this platform we executed toolboxes and scripts especially developed for the purpose of this study. The toolboxes featured the CSIRO SEAWATER toolbox (Phil Morgan & Steve Rintoul 1992), among others, such as M_Map (Rich Pawlowicz April 1997) and Tidal Model Driver for the OSU TOPEX/Poseidon Global Inverse Solution TPXO (2010 Egbert & Erofeeva, COAS). This last toolbox makes tide correction through the TPXO tide model based on the Laplace Tidal Equations, which uses altimetry data from the TOPEX/Poseidon satellite (TOPEX, 2014). It accounts for 10 harmonic and 3 non-linear components of the tide prediction equations. The

latest tide model was applied for our domain, for each RAPROCAN cruise, with a resolution of 0.25º.

All equations are according to the International System of Units (SI units). Henceforth, by applying the term "transport" we refer to volume transport and its SI units are $[m^3 s^{-1}]$ which is equivalent to 10^{-6} Sv.

To begin with, we drew simple Potential Temperature-Salinity ($\theta - S$) diagrams and vertical sections to glance at the CTD sampled data and identify water masses and possible eddy structures (section 4.1). Next, we extracted the dynamic height and the coordinates from the CTD data to compute geostrophic velocities (results in section 4.2) with the thermal wind equation of Marshall & Plumb (2008), through the dynamic method.

$$v_g(z) - v_g(z_1) = -\frac{g}{f}\int_{z_1}^{z} \frac{1}{\rho_0}\frac{\partial \sigma}{\partial x} dz = -\frac{g}{f}\frac{\partial D}{\partial x} \quad (1)$$

In the leftmost side of this equation we have the difference between two geostrophic velocities at different depth levels z and z_1, whereas the rightmost side of it show the zonal partial derivative of the dynamic height D multiplied by the negative factor of the gravitational acceleration g, divided by the Coriolis parameter f - which is explained further below. The other variables of equation (1) are: a reference density ρ_0 of ocean water of 1023 kg m^{-3} and a zonal partial derivative of potential density σ, which is vertically integrated

To apply the dynamic method we assume there are underlying adjacent and opposite flowing ocean currents. The method admits a layer between these two water masses where the flow must be zero. Based on other works done in this region before, such as Hernández-Guerra et al. (2005), Machín et al. (2006), Comas-Rodríguez (2011) or Pérez-Hernández et al. (2013), we use neutral density values to divide the water column into 12 different layers (table 2). Jackett & McDougall (1997) introduced this variable to reduce errors in deep ocean calculations, since potential density underperformed. Neutral density γ_n is defined as the scalar potential that satisfies:

$$\nabla \gamma_n = b\rho(\beta \nabla S - \alpha \nabla \theta) \quad (2)$$

where b is an integration factor, α and β are the thermal expansion and saline contraction coefficients, respectively, S is the Salinity and Θ the potential temperature. Table 2 also shows which water mass corresponds to a certain neutral density interval in the Canary Basin.

Table 2 – Neutral Density layers used in the analysis and the equivalent water masses per layer. The density values refer to the lower limit of each layer. Adapted from Pérez-Hernández et al. (2013).

Layer	Lowe Interface γ_n, (kg m^{-3})	Water Mass
1	26.8500	Surface water
2	27.1620	NACW
3	27.3800	NACW
4	27.6200	NACW
5	27.8200	MW/AAIW
6	27.9220	MW/AAIW
7	27.9750	MW/AAIW
8	28.0080	NADW
9	28.0440	NADW
10	28.0720	NADW
11	28.0986	NADW
12	28.1100	NADW

In agreement with Machín et al. (2006) we chose a level of no motion of 27.38 kg m^3 for the Lanzarote Passage and a value of 28.072 kg m^3 (from Pérez-Hernández et al. (2013)) for the remainder of the transect. These levels were obtained through inverse box models and should be more accurate than using γ_n layers at the interface between different water masses.

Our MATLAB script requires 3 input files, two control files – the transect is divided into the Lanzarote Passage and the rest - and one file with the neutral density values for each layer. Together with these files the CTD data are processed and a bathymetry file is generated, in order to obtain realistic geostrophic velocities at the slope of the ocean bottom (Rayner et al., 2011). We used two different bathymetry data sets: one that originates from Sandwell & Smith (1997), and another one from the M_Map toolbox – the Global Self-consistent Hierarchical High-resolution Geography, or GSHHS.

An axis rotation was applied to the current velocities, in the diagonal section of the transect, according to Protter & Protter (1988), with x,y as the original coordinates and a theta of -13.1º as the angle between the initial and the final axis.

$$\begin{cases} x' = x \cdot cos(\theta) + y \cdot sin(\theta) \\ y' = -x \cdot sin(\theta) + y \cdot cos(\theta) \end{cases} \quad (3)$$

The Ekman and Sverdrup transports were also calculated. The results are shown in sections 4.2, 4.4 and 5. The equations as they appear in Fraile-Nuez & Hernández-Guerra (2006) are:

$$V_{ekm} = \int \frac{-\tau^x}{\rho_0 f} dx \ [m^3 s^{-1}] \quad (4)$$

$$V_{sver} = \int \frac{rot(\vec{\tau})}{\rho_0 \beta} dx \quad (5)$$

Both transports are zonally integrated, since our stations are approximately aligned in one latitude. We will discuss the motivations of this choice later in section 4.2. The reference value of the ocean water density is written as ρ_0, as was already explained. Transports depend on the wind stress and consequently on a wind drag coefficient C_d. The respective formulas taken from Hernández-Guerra & Nykjaer (1997) are as follows:

$$C_d = \begin{cases} 1.14 * 10^{-3} & if\ |\vec{v}_{wind}| \leq 10\ ms^{-1} \\ (0.49 + 0.065|\vec{v}_{wind}|) * 10^{-3} & if\ |\vec{v}_{wind}| > 10\ ms^{-1} \end{cases} \quad (6)$$

$$\begin{cases} \tau^x = \rho_{air} C_d u_{wind} |\vec{v}_{wind}| \\ \tau^y = \rho_{air} C_d v_{wind} |\vec{v}_{wind}| \end{cases} \quad (7)$$

Here ρ_{air} is the reference surface air density and u, v are the zonal, meridional components of the wind at 10 m above the mean sea level. The curl of the wind stress is needed to compute the Sverdrup transport. Its equation, taken from Marshall & Plumb (2008) is:

$$rot(\vec{\tau}) = \frac{d\tau^y}{dx} - \frac{d\tau^x}{dy} \quad (8)$$

The Coriolis parameter f and its meridional derivative β were computed for the horizontal section of the transect. They depend on the angular velocity of the Earth's rotation Ω, the latitude φ and the Earth's radius a, according to the formulas from Marshall & Plumb (2008):

$$f = 2 \cdot \Omega \cdot \sin(\varphi) \tag{9}$$

$$\beta = \frac{df}{dy} = \frac{2 \cdot \Omega}{a} \cdot \cos(\varphi) \tag{10}$$

Both Sverdrup and Ekman transports were computed with the data points closest to the coordinates of the zonal segment of the transect. We found this to be the best strategy to compare the Sverdrup to the geostrophic transport, after testing this for various latitudes, among other things. Sverdrup transport is very sensitive to the wind stress curl values, with small spatial averaging or changes in latitude completely altering the outcome of the transport.

As for the Ekman transport, we simply calculate the accumulated transport at the La Palma longitude and then divided by the total summed distance of the correspondent accumulated transport. Henceforth, when we examine the accumulated transport we will always analyze it from East to West. By doing so, we assume that the Ekman transport is constant over the whole transect. Then we multiply by the individual distance between each RAPROCAN station point. This is the resultant Ekman transport for each station pair and it is then subtracted from each correspondent geostrophic transport per station pair, in order to respect the balance equation between the Sverdrup transport and the geostrophic transport:

$$V_{Sverdrup} = V_{geostrophic} + V_{Ekman} \tag{11}$$

(Fraile-Nuez & Hernández-Guerra, 2006).

After computing transport through geostrophic velocities we now want to assess the accuracy of the results by comparing them to the transport obtained using LADCP profiles (see section 4.3). We start by calculating the tide velocity components which will have to be removed from the velocity measured by the LADCP.

After the LADCP profiles are corrected, with the tide effect removed and with the local axis rotation applied, the relative velocities can be finally derived. For that, the geostrophic velocity graph is carefully compared to the LADCP one. If the graph is too noisy or if the two curves are too far apart, then the station is discarded and the respective reference velocity represented by not-a-number (NaN). Otherwise, a depth interval is chosen where the LADCP profile behavior is closer to the geostrophic velocity profile. The program will take the mean of those LADCP velocities and add it to the geostrophic profile. This way, a reference velocity is obtained, which is the actual velocity of the level of no-motion, resulting in a new, adjusted, geostrophic velocity profile.

LADCP velocities, like any other instrument measurements, have their associated uncertainty which will affect the new, adjusted, geostrophic velocity and, consequently, the transport yet to be computed. We took those uncertainties and calculated first of all the error propagation for the mean velocity between station pairs. This was followed by the estimate of yet another error propagation, this time of the mean velocity within the selected depth interval. Both propagations follow the next equation (Bell (2001), Averaging, Errors and Uncertainty):

$$error\ propagation = \frac{1}{N}\sqrt{\sum_{i=1}^{N} uncertainty_i{}^2} \tag{12}$$

For the first error propagation, N is the number of one pair of stations and the uncertainty is acquired directly from the LADCP data. This gives us one value per vertical level. For the second error propagation, N is the number of vertical levels of each individual depth interval, for each station pair. After these two estimates we end up with one error value per station pair, which is actually the uncertainty of the reference velocity. We can neglect geostrophic velocity uncertainties due to the good quality of CTD measurements and only have to account for the error of the reference velocity for the transport error. This way, the uncertainty of the transport is proportional to the reference velocity uncertainty (Averaging, Errors and Uncertainty):

$$a(x + \Delta x) = ax + a\Delta x \tag{13}$$

Finally, we computed the adjusted accumulated transport between station points. It is computed as an integral, with a gap for the Lanzarote Island. By summing the gamma layers by water mass (as grouped in table 2), we subdivided the transport into thermocline, intermediate and bottom layers and plotted them. Furthermore, we plotted the summed transport of all station pairs, for every gamma layer. We also plotted the net transport per layer, summed for the Lanzarote Passage only (at station 5).

For the 3 cruises with LADCP data we produced two kinds of curves for the net transport per layer to be able to establish a new layer of no-motion of 27.975 kg m^{-3} where the transport changes its direction in depth. With this new layer of no motion, we computed new geostrophic velocities and its resulting transport (results in section 4.4). This was only applied to stations 6 to 18, because the LP's chosen layer of no motion was accurately selected and did not need to be corrected.

In section 5 we discuss the obtained results and examine the variability of the calculated transport. Due to the fact that the analyzed RAPROCAN cruises did not cover all the season, we had to find an alternative way to group the cruises in order to understand their seasonal variability. This resulted in the following arrangement: February, August, fall (September & October) & December. We decided not to group December and February as winter because the trade wind regime, responsible for the current dynamics, is not the same.

We also discuss the relationship between the Atlantic MOC and the EBC variability. In this context, we compared transport computed through inverse box models by Machín et al. (2006), Hernández-Guerra et al. (2005) and the accumulated transport at different points of our transect to the monthly averaged UMO time-series. The UMO was found to be better correlated to the eastern boundary than the Atlantic MOC itself by various researches, including Pérez-Hernández et al. (in prep.), which is why we chose only to compare our results to the UMO transport. Both UMO and Canary Current transports were standardized according to Jolliffe (2002):

$$x(standardized)_i = \frac{x_i - \bar{x}}{\sigma} \tag{14}$$

Here x_i is the transport at time i, $\bar{x}$ is the average transport in time and σ is the corresponding standard deviation. Standardization implies that the resultant transports at time i have 0 mean and standard deviation of 1. This allows us to correctly compare different kinds of variables.

4. Results

4.1 Water mass identification

Near the Canary Archipelago, the existent water masses are the North Atlantic Central Water (NACW), the Antarctic Intermediate Water (AAIW), the Mediterranean Water (MW) and the North Atlantic Deep Water (NADW) – if a certain depth is reached (Machín et al., 2006). To identify these water masses and to check their temporal and spatial variation we analyze the potential temperature-Salinity (Θ-S) diagrams in figure 2 and the vertical sections of figure 3. The different colors of the plotted values in figure 2 refer to sampling in the Lanzarote Passage (blue) and to the remainder of the transect (black).

We can clearly see the presence of the four described water masses: NACW has the highest temperature and salinity values, whereas NADW reaches the lowest values depicted in figure 2. AAIW and MW can be seen in the center of the graphs, where the dots are more scattered. Blue dots in the 5-10 ºC interval represent AAIW and black dots in the same interval portray waters more similar to MW.

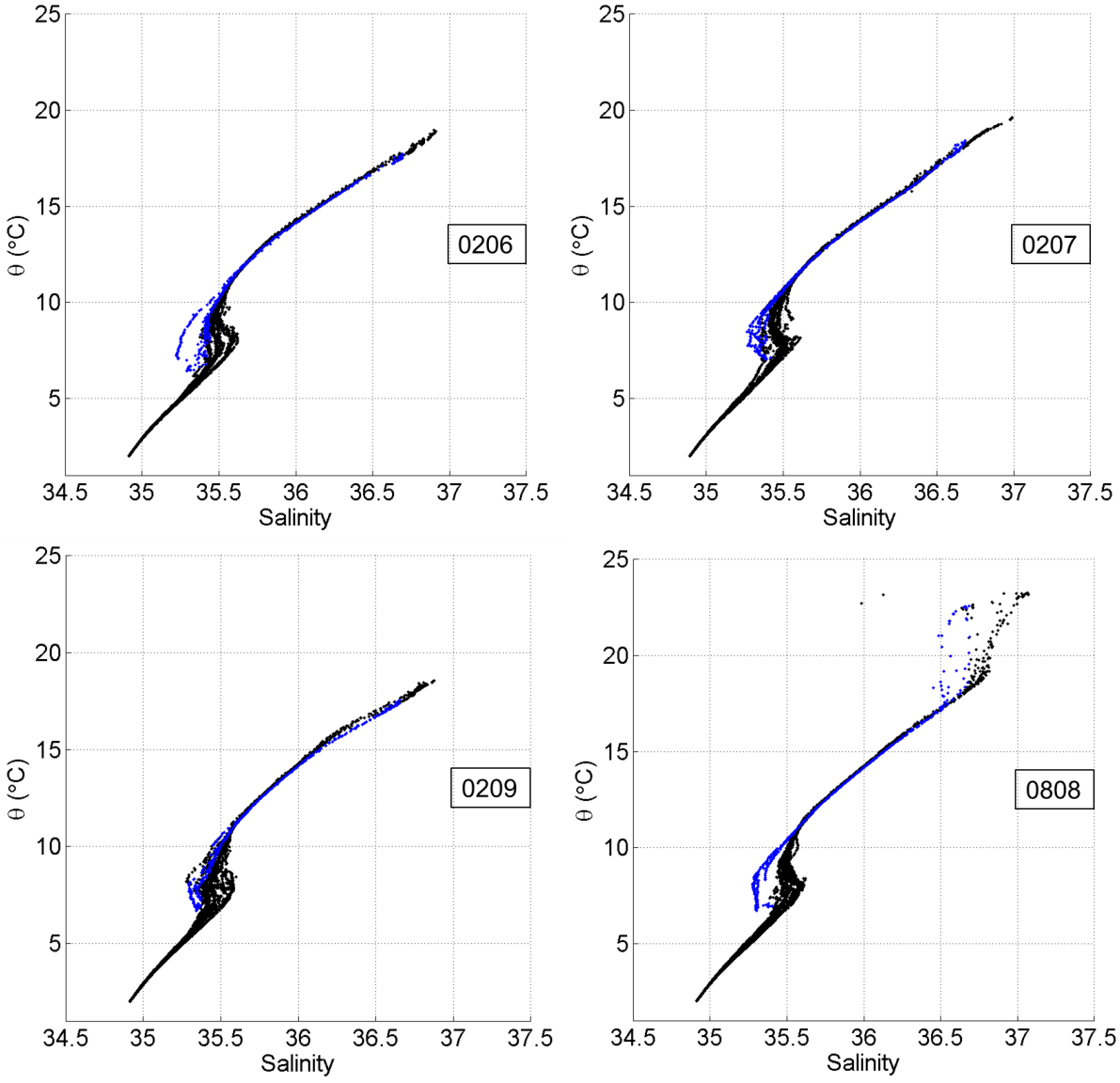

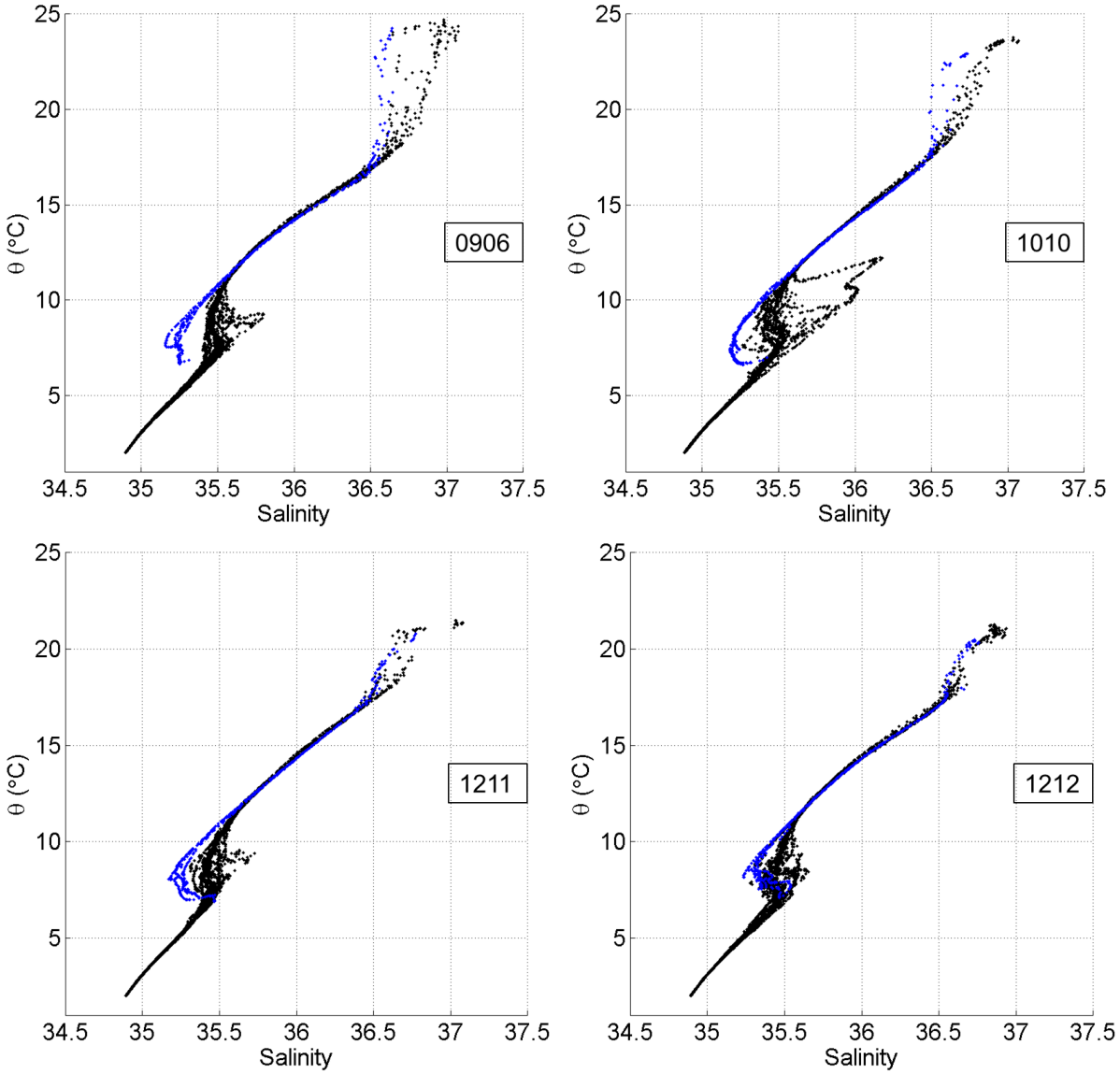

Fig. 2 – Θ-S diagrams. Blue - Lanzarote Passage waters, black – waters of the rest of the transect. RAPROCAN cruise period can be identified in the center-right part of each graph.

We can see that there are no significant changes throughout the seasons, except for the mixed layer of surface waters and when some random cruise has a peak of warm, salty water, as a sign of a Mediterranean eddy (Meddy) presence. Also, notice that the Lanzarote Passage waters are always less salty than the rest of the respective transect waters, with purer AAIW. This is visible throughout all months, regardless of the direction of the flow (see figure 12) due to the stretching of the Intermediate layers as described in Machín & Pelegrí (2009). This comes to show that AAIW can be found northward of the Canary Archipelago throughout the year, near the African coast.

Figure 3 confirms and completes the analysis described above, with each row representing a different RAPROCAN sampling period and each row a different variable – Potential Temperature, Salinity and Neutral Density. Evidence of upwelling can be seen in the potential temperature vertical section for the February cruises: the upper isothermal is not visible in the Lanzarote Passage, where there is colder upwelled water than in the rest of the transect.

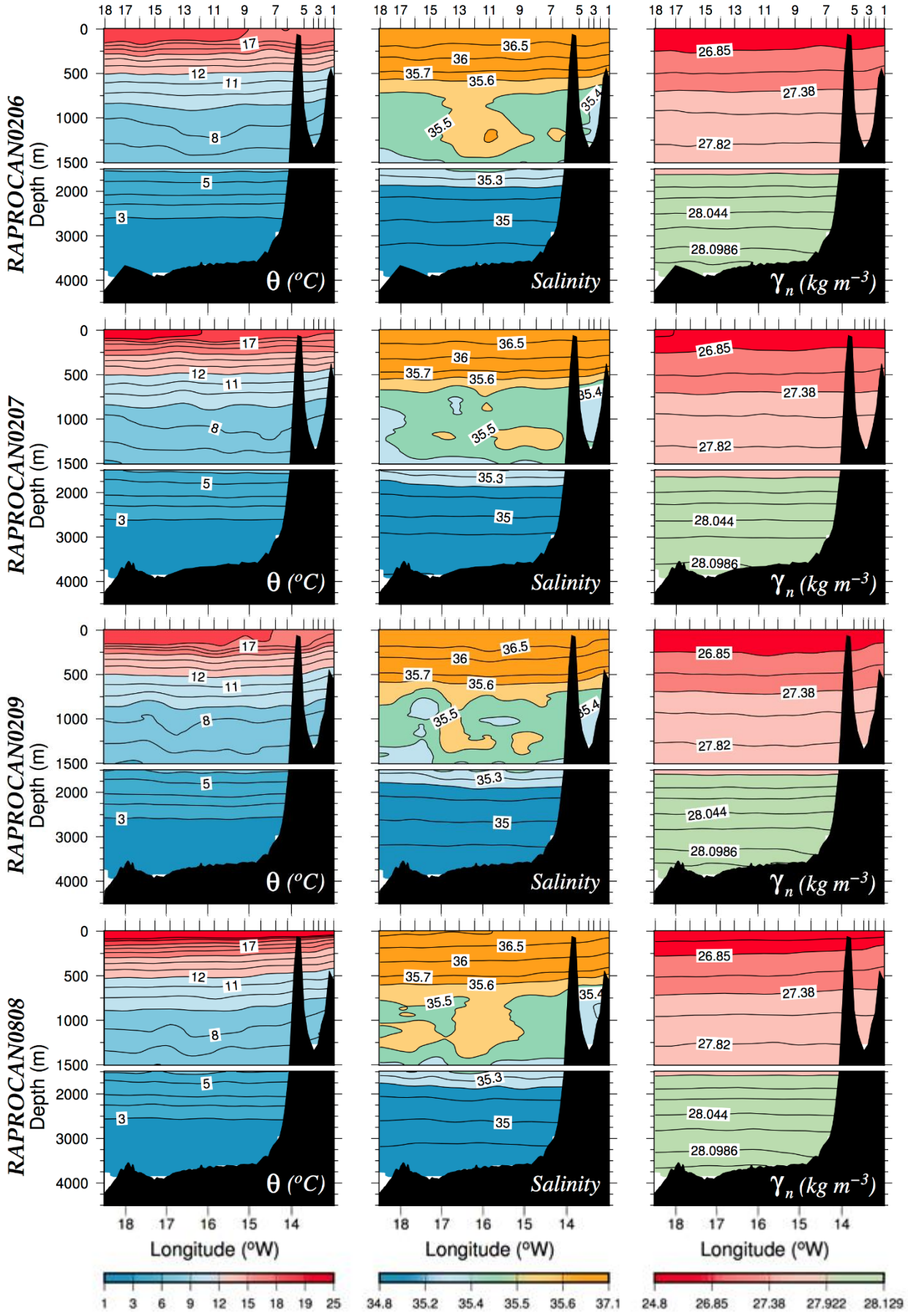
RAPROCAN0206
RAPROCAN0207
RAPROCAN0209
RAPROCAN0808
Depth (m)
θ (ºC)
Salinity
γn (kg m−3)
Longitude (ºW)

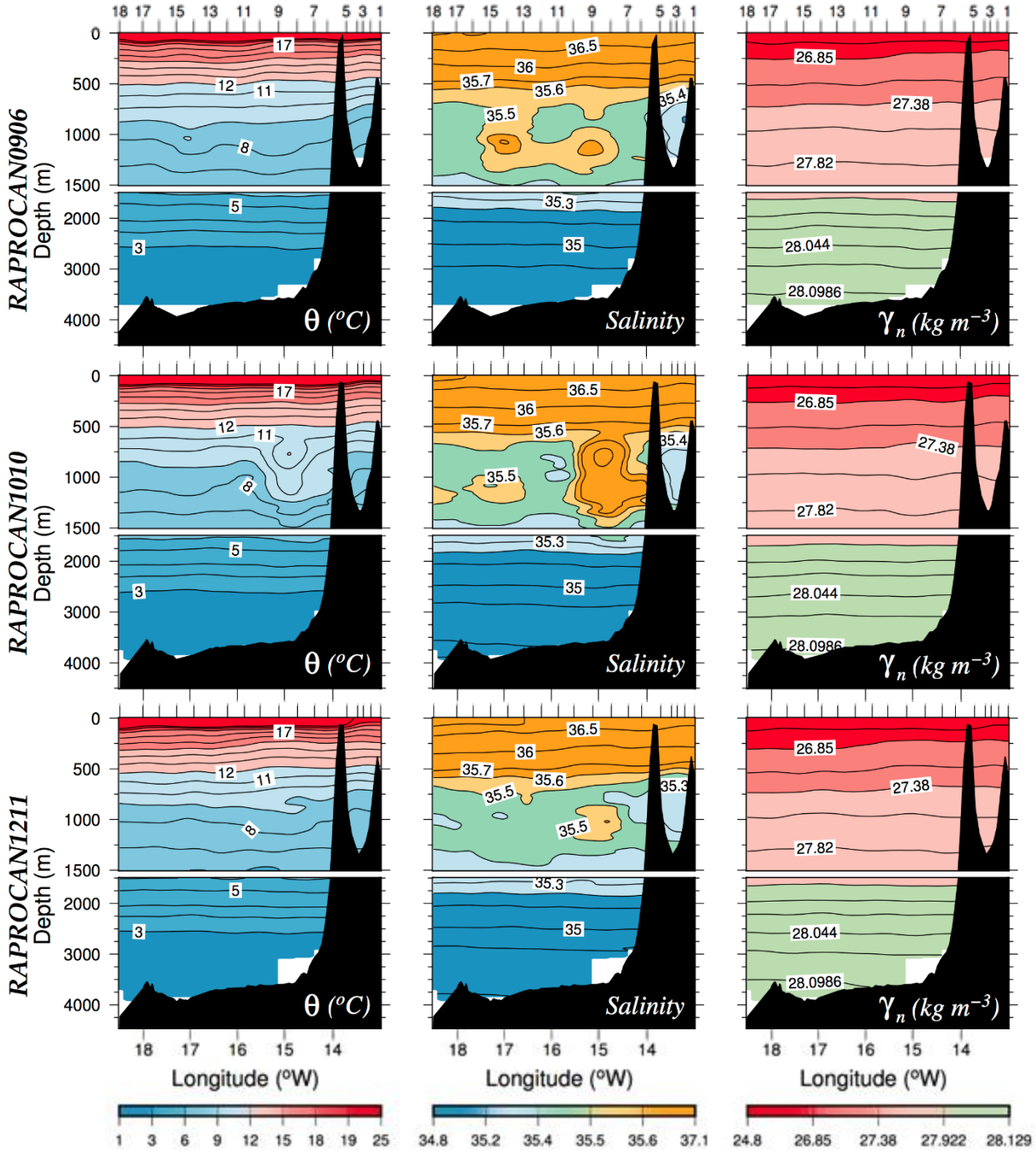
RAPROCAN0906
RAPROCAN1010
RAPROCAN1211
Depth (m)
θ (ºC)
Salinity
γn (kg m−3)
Longitude (ºW)
18 17 15 13 11 9 7 5 3 1
18 17 16 15 14
0 500 1000 1500 2000 3000 4000
1 3 6 9 12 15 18 19 25
34.8 35.2 35.4 35.5 35.6 37.1
24.8 26.85 27.38 27.922 28.129

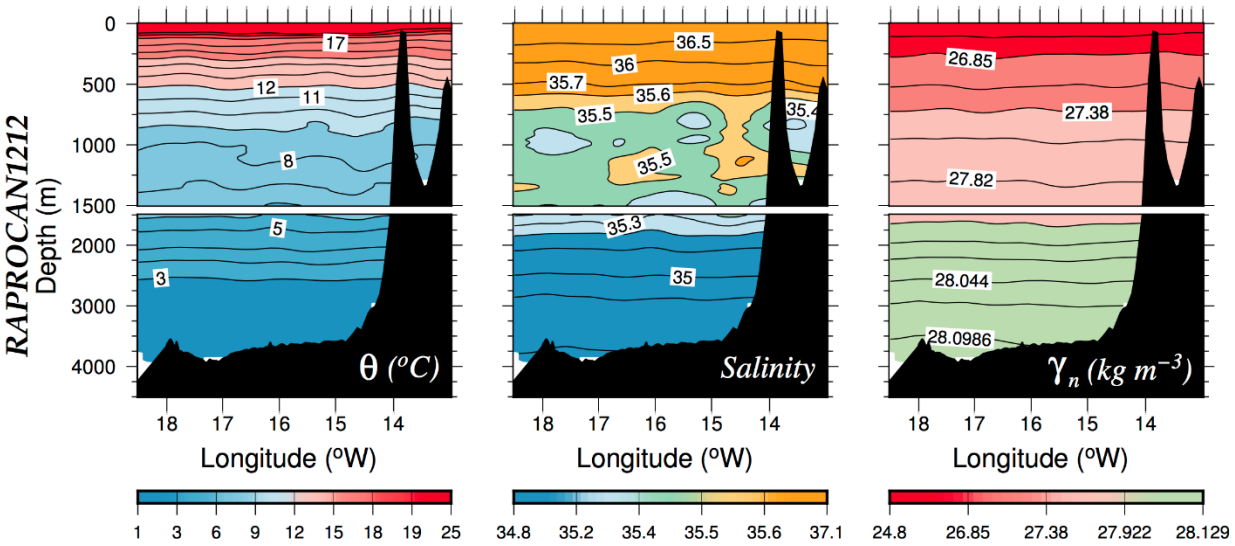

Fig. 3 – Vertical Sections of different water properties, as labeled in the bottom right corner of the graphs. Correspondent color bars are at the bottom of each column. Each row corresponds to a different RAPROCAN cruise, labeled on the left side of the depth scale.

We can find another hint on the Meddy presence in the vertical sections of potential temperature and of salinity in the October campaign. Notice how a saltier water core extents from 500 m to 1500 m west of Lanzarote. It corresponds to the position of a warmer water core centered at approximately 1000 m. This is the same cruise which has a peak of colder, saltier water in figure 2.

Otherwise, the water mass characteristics and distributions have no special features. The neutral density vertical sections of figure 3 show a well stratified ocean for all cruises. Temperature ranges from approximately 2 ºC under 3000 m to 18 or 25 ºC at surface, depending on the season. Isolines under 16 ºC do not seem to shift seasonally in depth. Salinity varies between 34.8 and 37.1, from ocean bottom to surface respectively, with the discontinuities in the 500-1500 m interval due to the presence of saltier cores of water.

4.2 Geostrophic velocities and initial transport

In the next figure we will present cross sections with geostrophic velocity contours, with northward flow represented in blue and southward shown in red. The geostrophic velocity computed through the described dynamic method in section 3 is only the baroclinic component of ocean current (Apel, 1999). There is yet no perfect technique to obtain the exact, absolute velocity of the ocean current in the deep ocean (Comas-Rodríguez et al., 2010). Also, the choice of the level of no motion has not an unequivocal definition, but we assume that the latest studies are close to the real value.

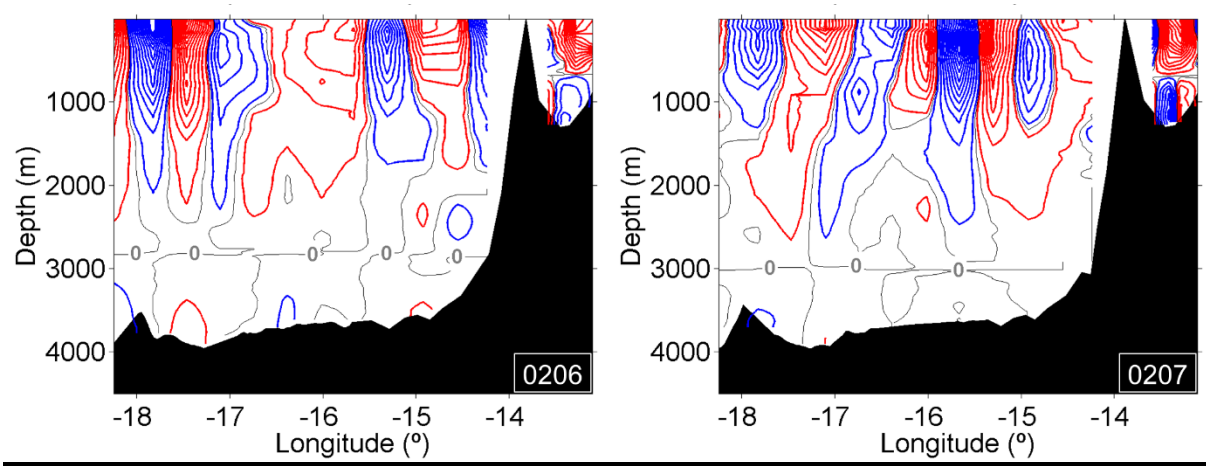

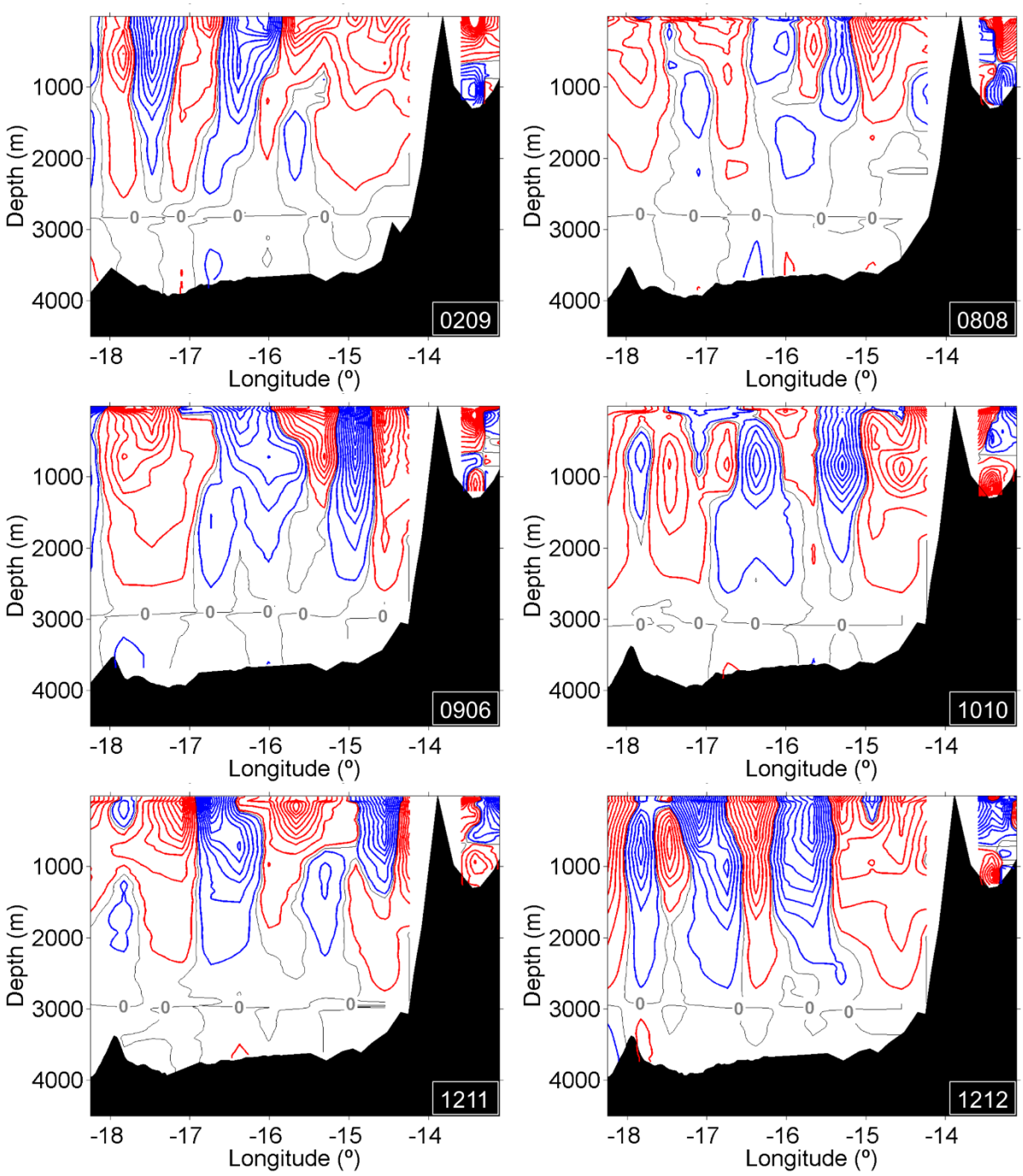

Fig. 4 – Geostrophic velocity contours, with bathymetry shaded in black. RAPROCAN cruise period can be identified in the bottom right corner of each graph. Blue – northward flowing current, red - southward flow, grey - zero velocity. Isolines with 1.5 cm/s spacing.

One of the most obvious things we can observe for figure 4 is that the horizontal line formed by the zero velocity isolines around the depth of 3000 m is an artifact of our chosen layer of no motion. This contour line oscillates around this depth from cruise to cruise in the same manner that the gamma layer of 28.072 kg m^{-3} does. Moreover, the dynamics of the Lanzarote Passage are clearly visible here, since the poleward current is at the bottom of the passage during February and August, whereas in December it's at the surface, with a transition phase in fall. Otherwise, only a complex structure of cells with adjacent, opposite flows are visible here.

To accurately compare the geostrophic transport with the Sverdrup transport as proposed in section 3, we must first calculate the Ekman transport to have it subtracted from the top layer

of the geostrophic transport. Table 3 shows the Ekman transport in Sverdrup for each of the RAPROCAN cruise periods. The last column gives the mean Ekman transport of the Canary Basin.

Table 3 – Accumulated Ekman transport at 18.5º W, for each RAPROCAN cruise period. Units in Sv.

0206	0207	0209	0808	0906	1010	1211	1212	Mean
-0.07	0.09	0.00	0.30	0.09	0.13	0.37	0.06	0.12

Given the trade wind variability, Ekman transport should be greater in high summer, where winds are most intense (Pacheco & Hernández-Guerra, 1999), although there is evidence of a second maximum in northward Ekman transport around January (Atkinson et al., 2010). Comparing 0808 to 0906 and 1010 we can see that these years wind field behave as expected, that is, they lose strength after summer. Knowing that trade winds are easterlies, Ekman transport should always be positive, since Coriolis force deflects the current to the right in the northern hemisphere. This is not the case for 0206. 0209 is also abnormal since it shows no meridional Ekman transport. Machín et al. (2006) and Pérez-Hernández et al. (2013) also found southward Ekman transport in this region, possibly due to the passing of a Low Pressure system during winter (Pelegrí et al., 2005). Last of all, transport in 1211 is rather strong for that season, compared to the value obtained by Machín et al. (2006).

The transport obtained after including the Ekman contribution in the initial velocities of figure 4 can be seen in figure 5 as the transport per layer and in figure 6 as the accumulated transport per station pair.

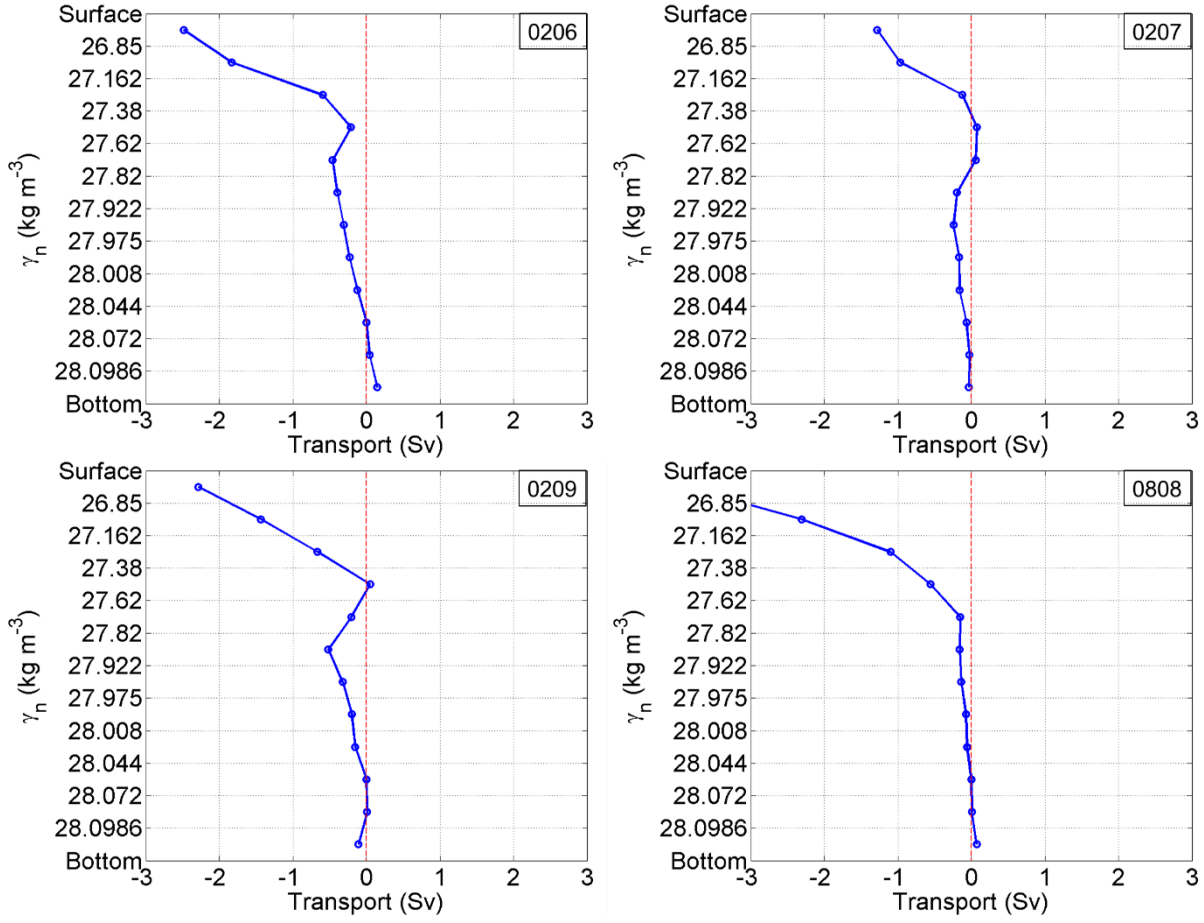

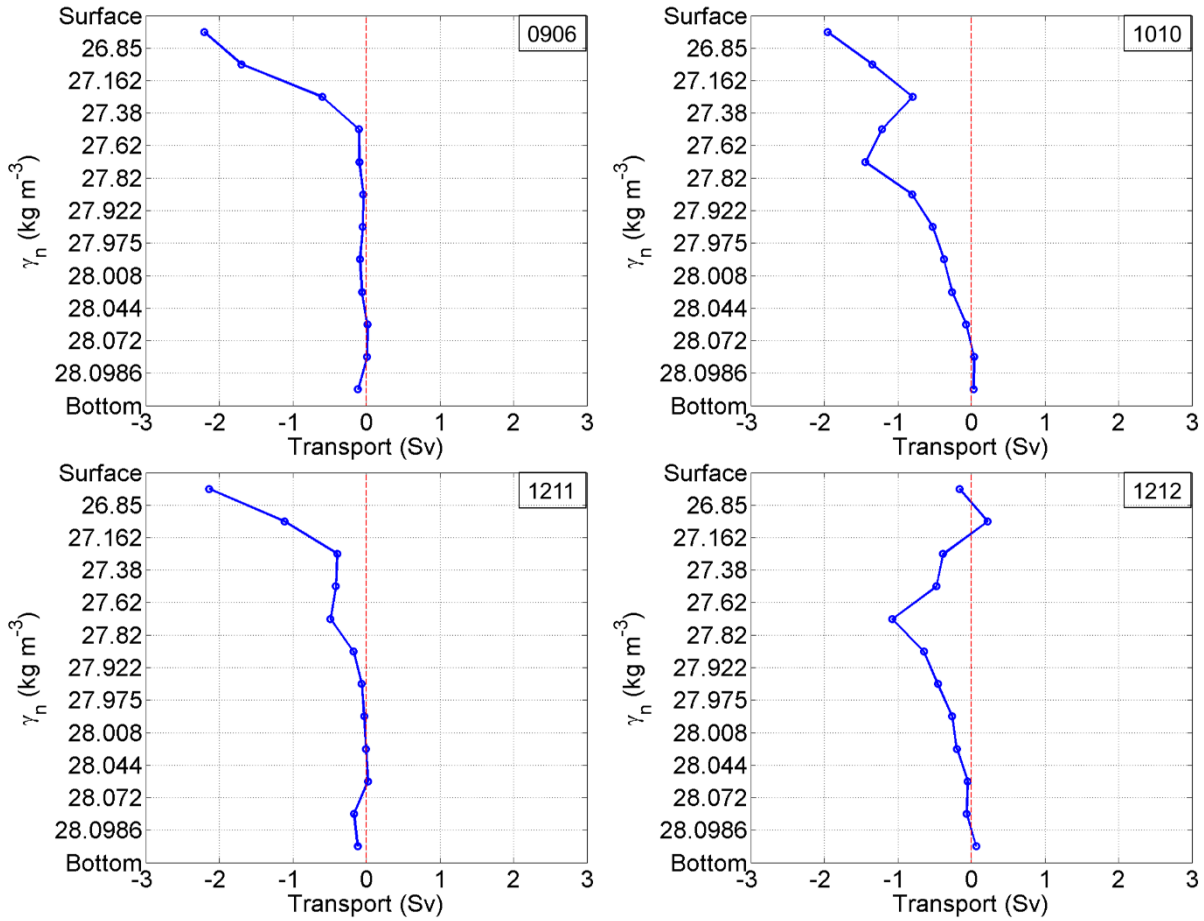

Fig. 5 – Initial net transport per neutral density layer. RAPROCAN cruise period can be identified in the top right corner of each graph.

The main net transport according to the figure is always to the south (always negative). Transport is always strongest at surface, with the exception of 2012. The relative minimum at the 27.82 layer, for 1010, is explained by the presence of the Meddy already identified before. In these graphs we can see how the transport decreases slowly to zero in the chosen layer of no motion, although the layer itself at which this happens is an artifact.

As we can see, the Ekman transport of table 3 is at least one order of magnitude smaller than the transport depicted here. For this reason, we find that calculating only one component of the Ekman transport is good enough and only use wind stress values at the latitude of the main segment of our transect.

The small surface transport in December 2012 will now be clarified through figure 6, where we can see the accumulated transport per station pair. This next figure has three different lines, one for each group of layers according to their neutral density level interval, as is shown in table 2. The red line represents the thermocline transport, whereas the green one represents the intermediate transport. Finally, the blue lines shows the deep transport. The gap at approximately -14º of longitude corresponds to the position of the Island of Lanzarote in our transect, separating the transport of the Canary Upwelling Current, in the LP, and the transport of the main branch of the Canary Current in the rest of the transect.

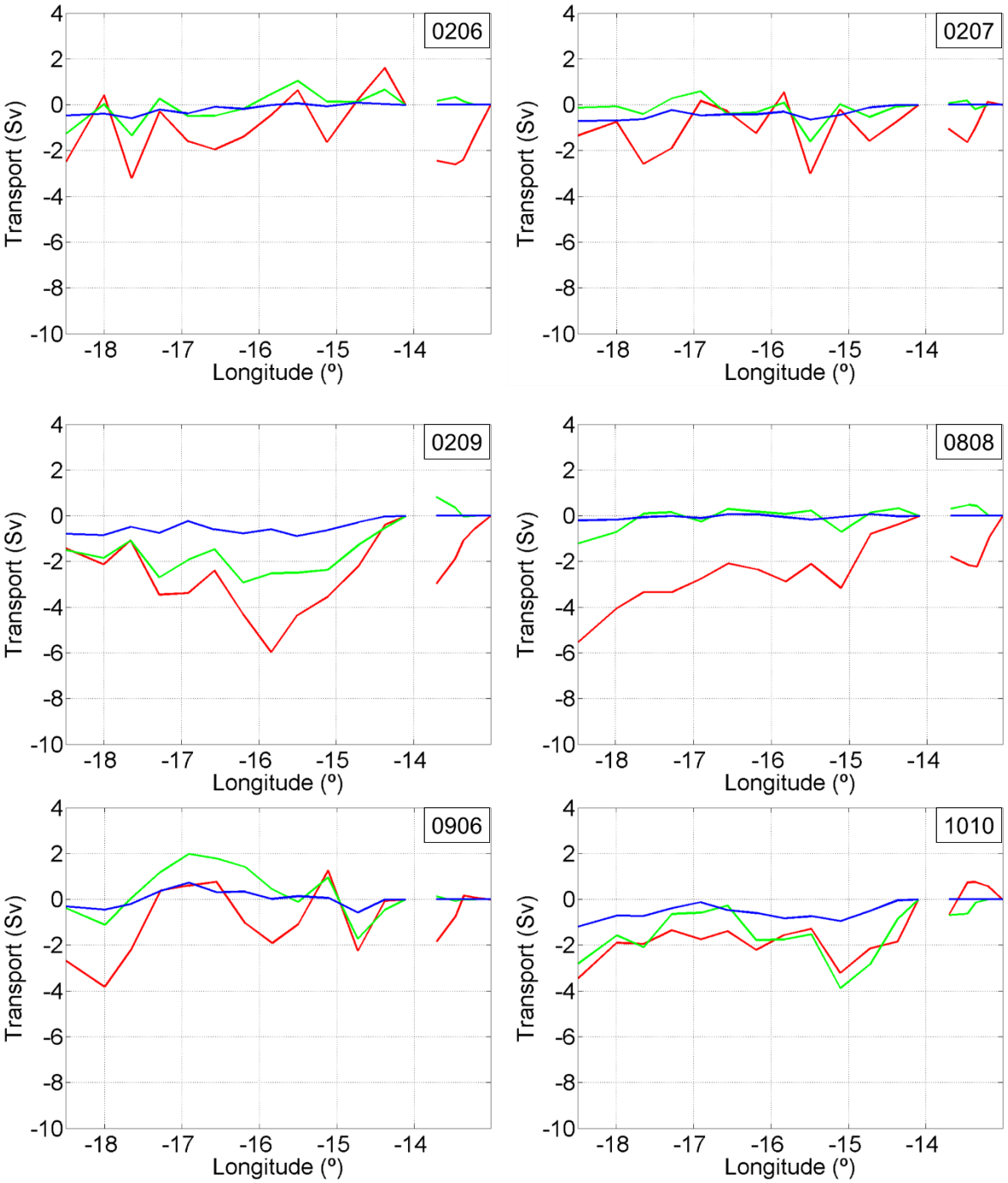
0206
0207
0209
0808
0906
1010
Transport (Sv)
Longitude (º)
4
2
0
-2
-4
-6
-8
-10
-18
-17
-16
-15
-14

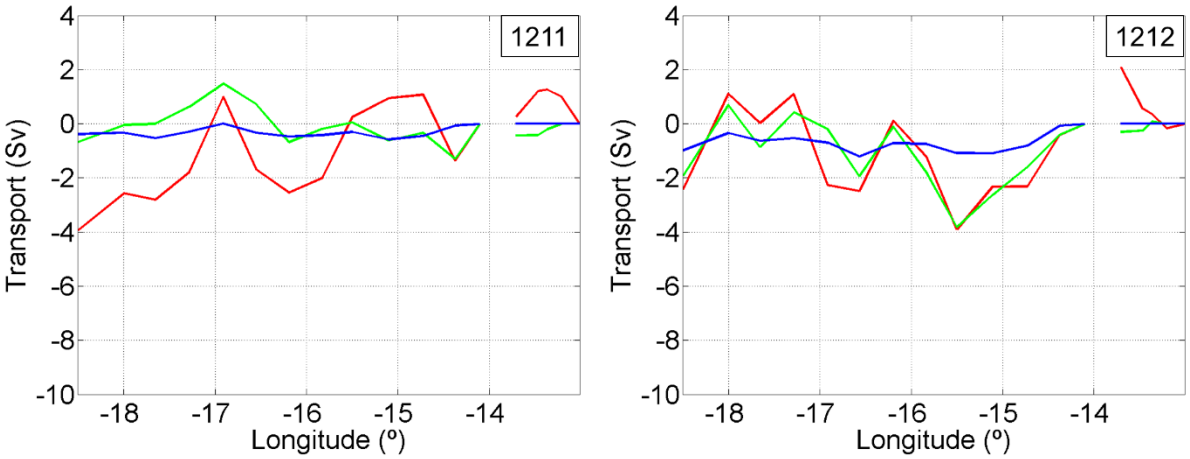

Fig. 6 – Initial accumulated transport per station pair. RAPROCAN cruise period can be identified in the top right corner of each graph. Grouped layers: red – from surface to 27.38 kg m^{-3} gamma layer; green – 27.38 to 27.922 kg m^{-3} gamma layers; blue – from 27.922 kg m^{-3} to bottom.

Notice that here, the intermediate transport is smaller and less variable than the surface and bottom transports. This is an artifact of the chosen layer of no motion, and should not be given much importance in this sense. Here we will focus only on the surface transport, for the Lanzarote Passage and for the rest of the transect. The abrupt,alternating peaks in the transport suggest the presence of eddies, as was identified in Mock (2011) and Comas-Rodríguez (2011), cyclonic if it is an uppward peak and anticyclonic if its downward.

Usualy the Canary Upwelling Current transport is negative, meaning a southward flow in the first 5 months. Then it changes into a northward motion in the last two cruises, with a clear transition fase in the October. This is not exactly like the results of Fraile-Nuez et al. (2010). Their study showed a northward transport during fall, with a transition phase in December. Nevertheless, if we take a look at their transport of the individual years, we can see that the inversion is sometimes too weak to be noteworthy or it's occurance period shifts ahead. This is probably related to the wind regime in the area. If the trade winds' maximum strength takes place sooner or later it would alter the period where the southward flow is distabilized due to a high positive vorticity. This positive vorticity would mean an offshore displacement of the current in order to maintain absolute vorticity, and consequently the surfacing of a near-surface poleward undercurrent (Pelegrí et al., 2005).

For the rest of the transect, if we smoothen the effects of the eddies in the transport, we can clearly see that there is always a negative tendency, from station 6 to 18 (i.g. from 14.1º to 18.5ºW). This means that the surface waters at the transect have and overall southward movement, as is expected for the eastern boundary current of the NASG (Marshall & Plumb, 2008) (Pedlosky, 1996), eventhought, at times, the transport is locally positive. Furthermore, the graphs tell us that the largest net transport is in August, which is in accordance with the strenghtening of the trade winds at that month.

4.3 LADCP adjusted transport

Next step of this study is to assess how well geostrophic velocities actually describe the flow in the ocean, through the use of LADCP. The tide only slightly affects the LADCP velocity but it should not be neglected. This can be verified by comparing the meridional tide component shown in figure 7 with the velocity profiles of figure 8.

The tide velocity always oscilates around zero throughout the transect. Otherwise, there are no important features about the meridional tide component worth mentioning.

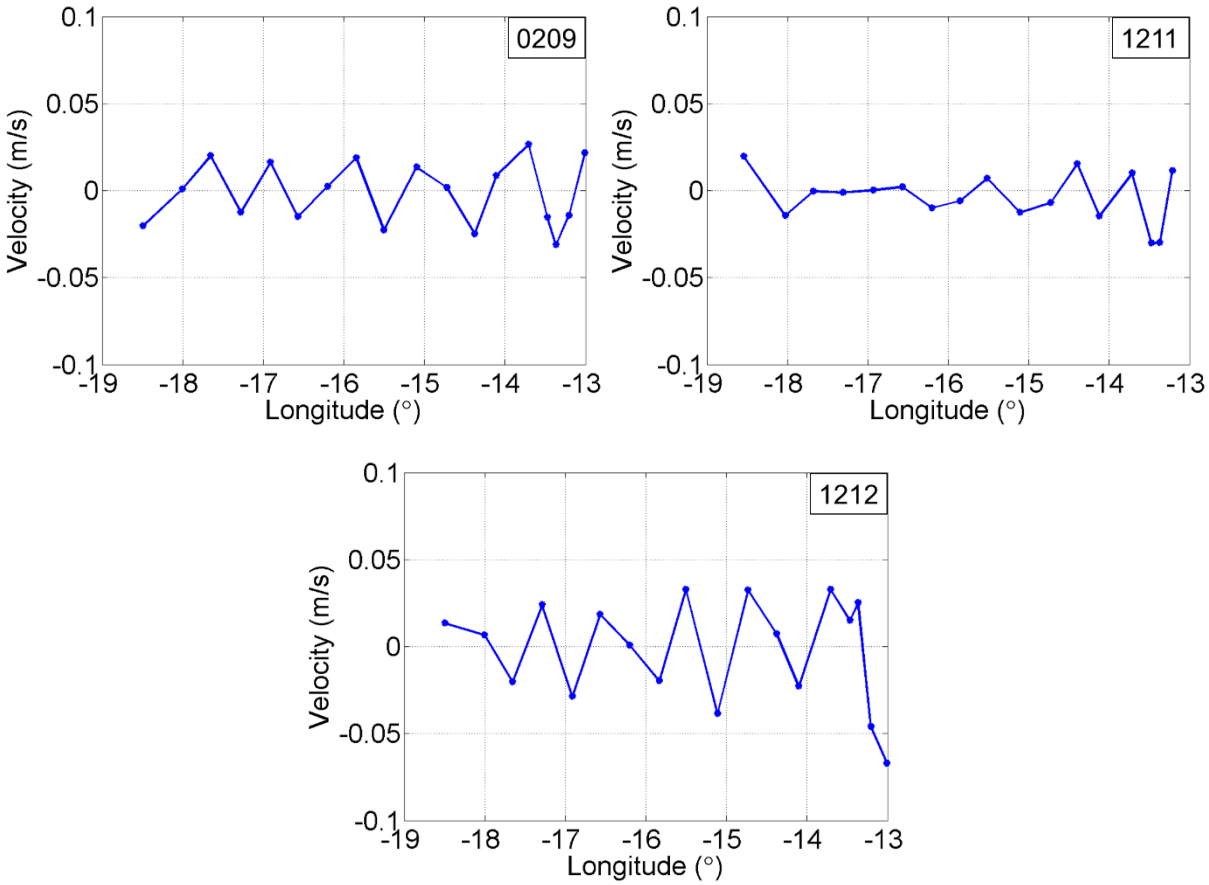

Fig. 7 – Tide meridional component retrieved from global model TPXO 7.2. RAPROCAN cruise period can be identified in the top right corner of each graph.

Below we can see an example of a LADCP profile and the adjusting of the geostrophic velocity profile. For this station pair, the tide velocity would be approximately 0.02 m/s, which would clearly affect the LADCP. One can see that the adjustment of the profile is somewhat subjective, for the LADCP is very noisy, especially above 1500 m in this case. The difference between the geostrophic transport with the Ekman component (bold black line) and the adjusted geostrophic transport (dashed black line) of figure 8 gives us the relative velocity, which is actually the barotropic component of the ocean current (Apel, 1999).

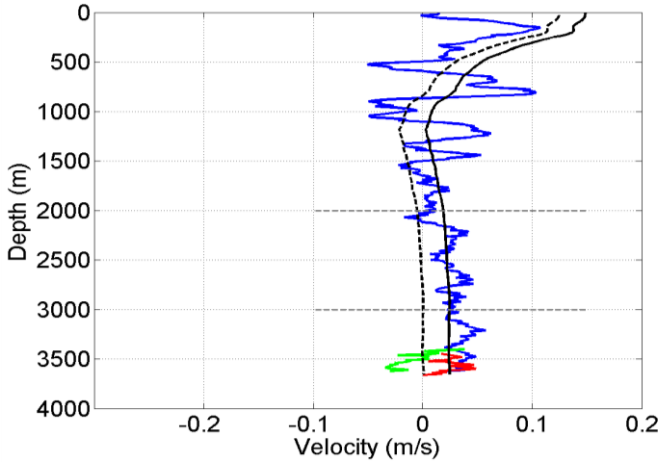

Fig. 8 – Example of adjustment of geostrophic velocity profiles to LADCP velocity profile. Station pair 11-12 of RAPROCAN cruise 0209. Blue - LADCP velocity; dashed black - geostrophic velocity; black - adjusted geostrophic velocity; green & red - bottom LADCP velocities, for each of the stations composing the station pair; grey, horizontal dashed lines - interval chosen for adjustment.

The following figure illustrates the reference velocities computed through the LADCP velocity adjustment, with the respective error bar for each station pair. As can be deduced from this figure, there were many of the LADCP profiles that could not be used for the adjustment, especially in the 1211 cruise. We must take this into account when comparing, in figures 12 & 13, the adjusted transport to the initial transport of this specific cruise.

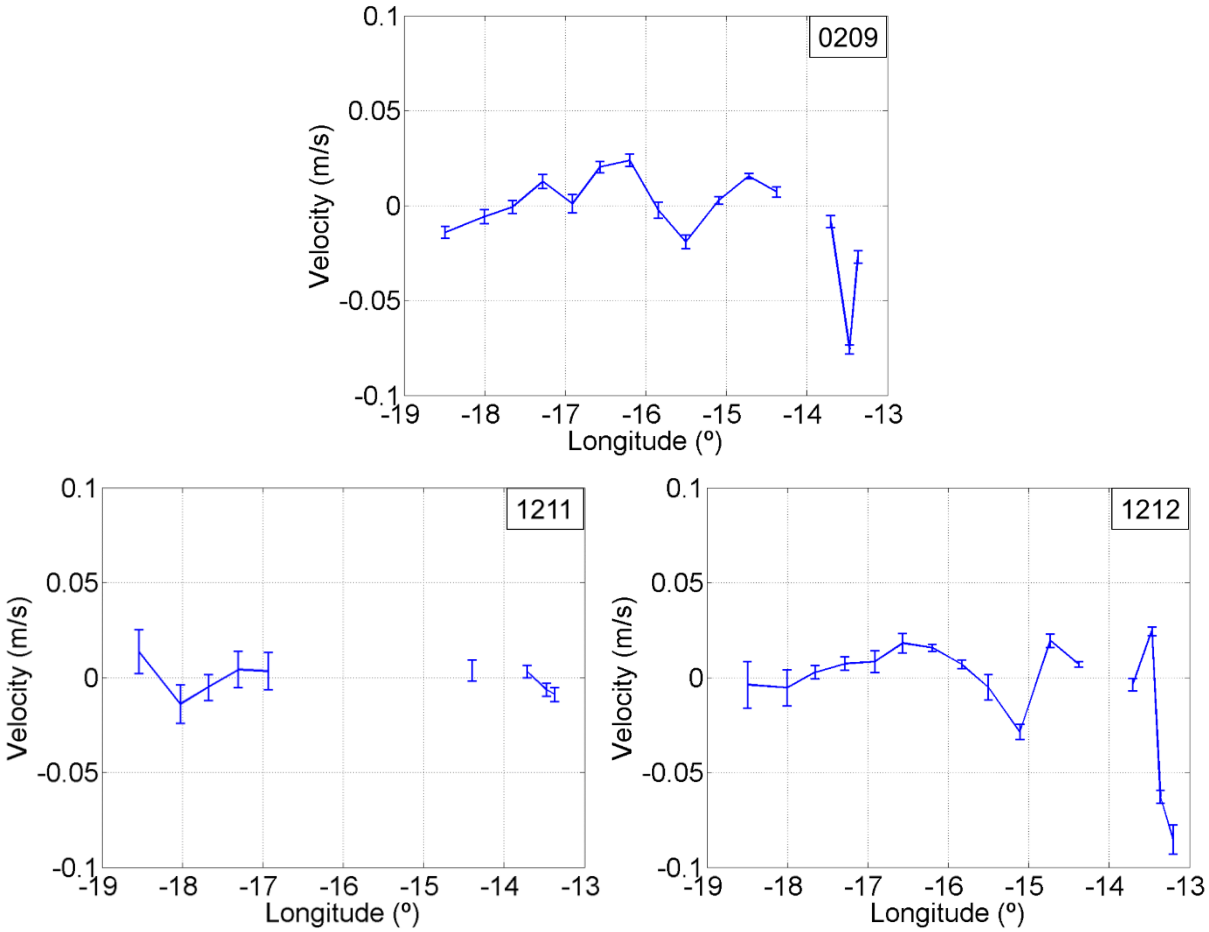

Fig. 9 – Reference velocities and error bars. RAPROCAN cruise period can be identified in the top right corner of each graph. Gaps either for Lanzarote at longitude 14º W or for discarded stations.

Another thing worth noticing is the fact that reference velocities are usually greater in the LP. This could be due to the fact that its removed tide component was not as accurately predicted as for the rest of the transect due to the changing bathymetry (Egbert & Erofeeva, 2002). However, the most probable explanation for these higher reference velocities is that the Lanzarote Passage is shallower and narrower than the rest of the transect and has therefore stronger currents. Consequently, the depth interval from which the reference velocities are derived is also shallower, with currents with high variability in speed and direction, which surely must affect the resulting reference velocities.

If we assume that these reference velocity values are realistic, then the barotropic component of the current must be stronger in an along-slope context. Since Aaboe et al. (2009) found evidence of this behavior in the Nordic Seas, it would be very interesting to carry out, in the future, a similar analysis in an EBC context.

We will now move on to show the consequent transport of the described adjustment.

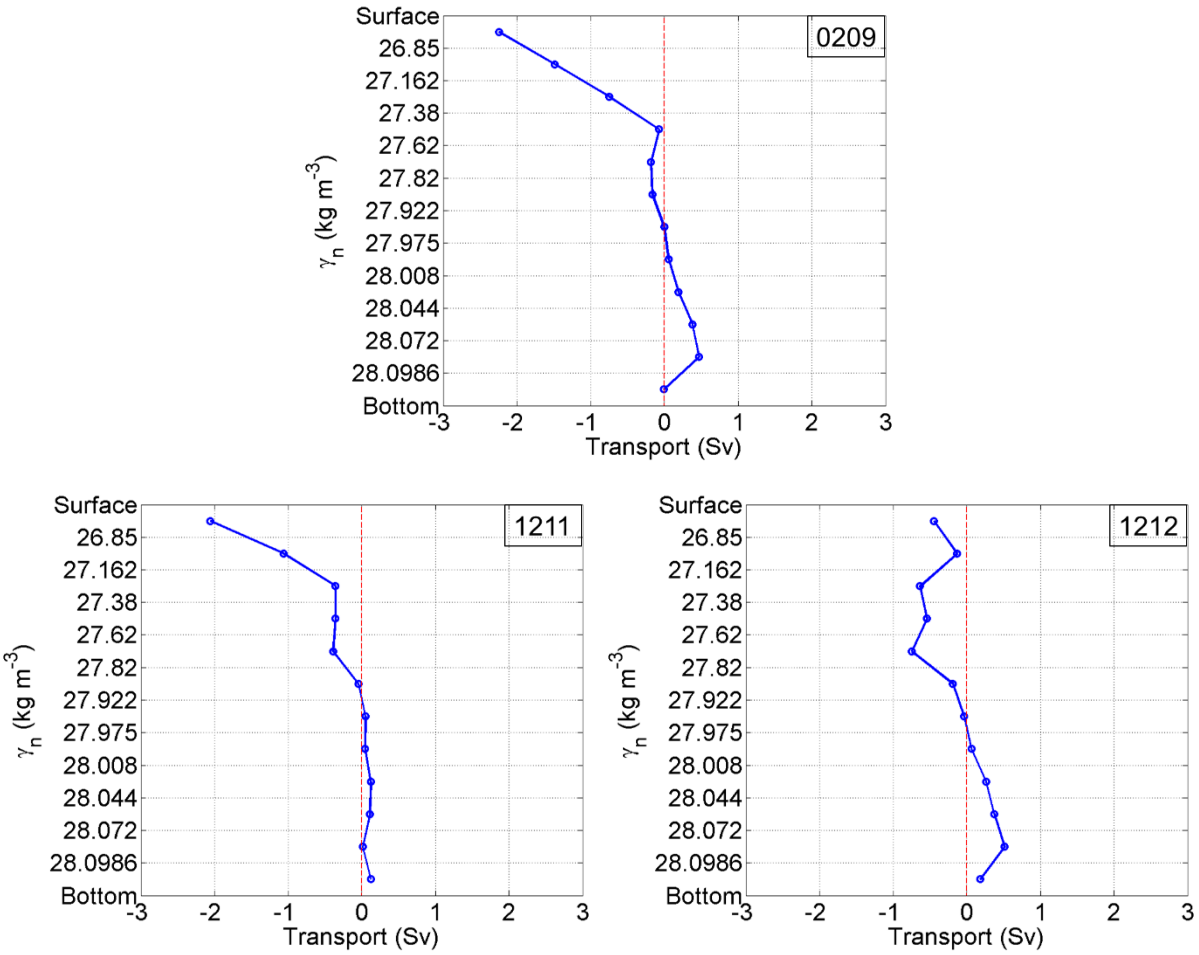

Fig. 10 – Adjusted net transport per neutral density layer. RAPROCAN cruise period can be identified in the top right corner of each graph.

Notice in figure 10 how the adjusted net volume transport in the first layers is always southward whereas in the bottom layers it flows poleward. The neutral layer where the transport changes sign is essentially the same in every cruise, 27.975 kg m^{-3}, resting above the selected layer of no motion. We must keep in mind that this represented transport is a summed transport, not a mean transport and therefore not affected by the higher reference level of no-motion of the Lanzarote Passage. This is a crucial detail in this study, for it allows us to correctly choose the new layer of no motion and to obtain a more realistic transport.

Before we get to the results of this new layer of no motion, we will show the results for the adjusted accumulated transport per station pairs, with the same color scheme as in figure 6.

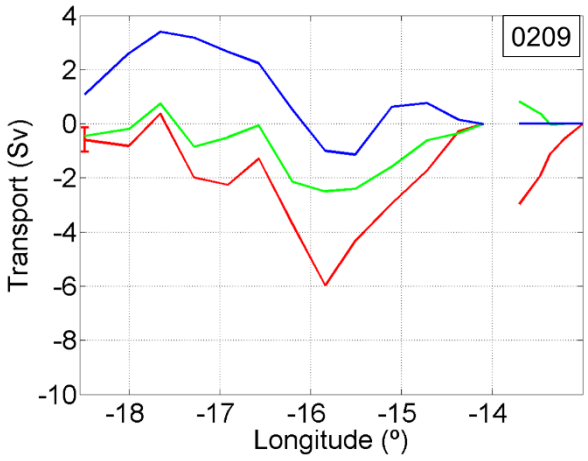

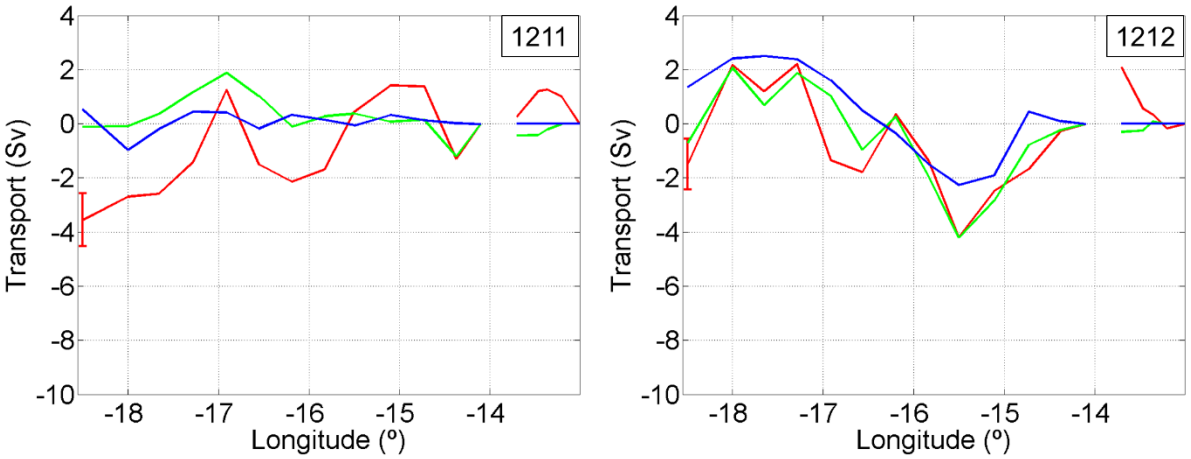

Fig. 11 – Accumulated, adjusted transport per station pair. RAPROCAN cruise period can be identified in the top right corner of each graph. Color legend is the same as figure 6. Uncertainties for 0209, 1211 and 1212 are 0.5 Sv, 1.0 Sv and 0.9 Sv respectively.

When figure 11 is compared to the respective graphs in figure 6, we can observe that the LADCP adjusted velocities mainly affects the bottom layers. Therefore, we can compare the surface layer transport from period to period even for the cruises without LADCP data.

4.4 Final transport and new layer of no-motion

To better visualize the particular dynamics of the Lanzarote Passage, we will now show the net transport per layers only from stations 1 to 5. The cruises with available LADCP data have two curves, one for the transport with and the other without the LADCP adjusted velocities.

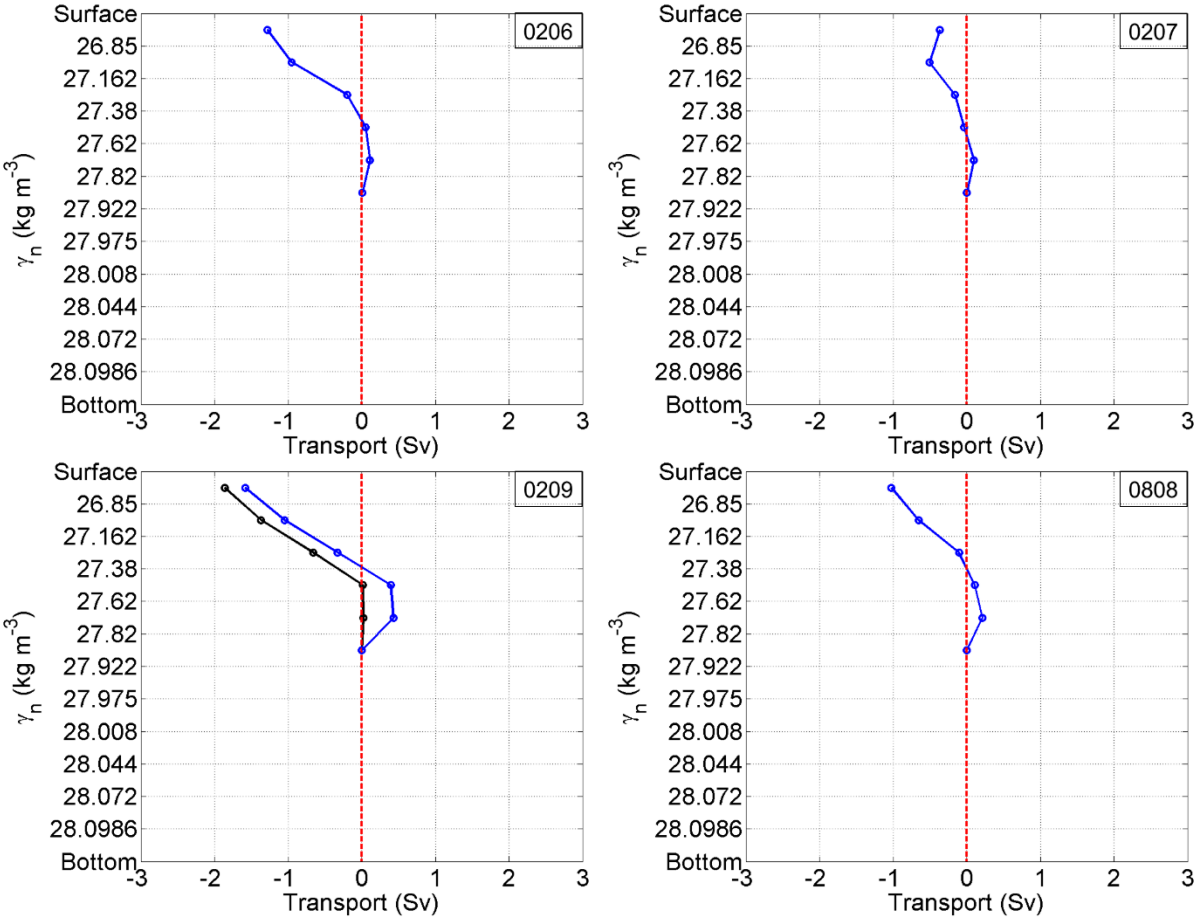

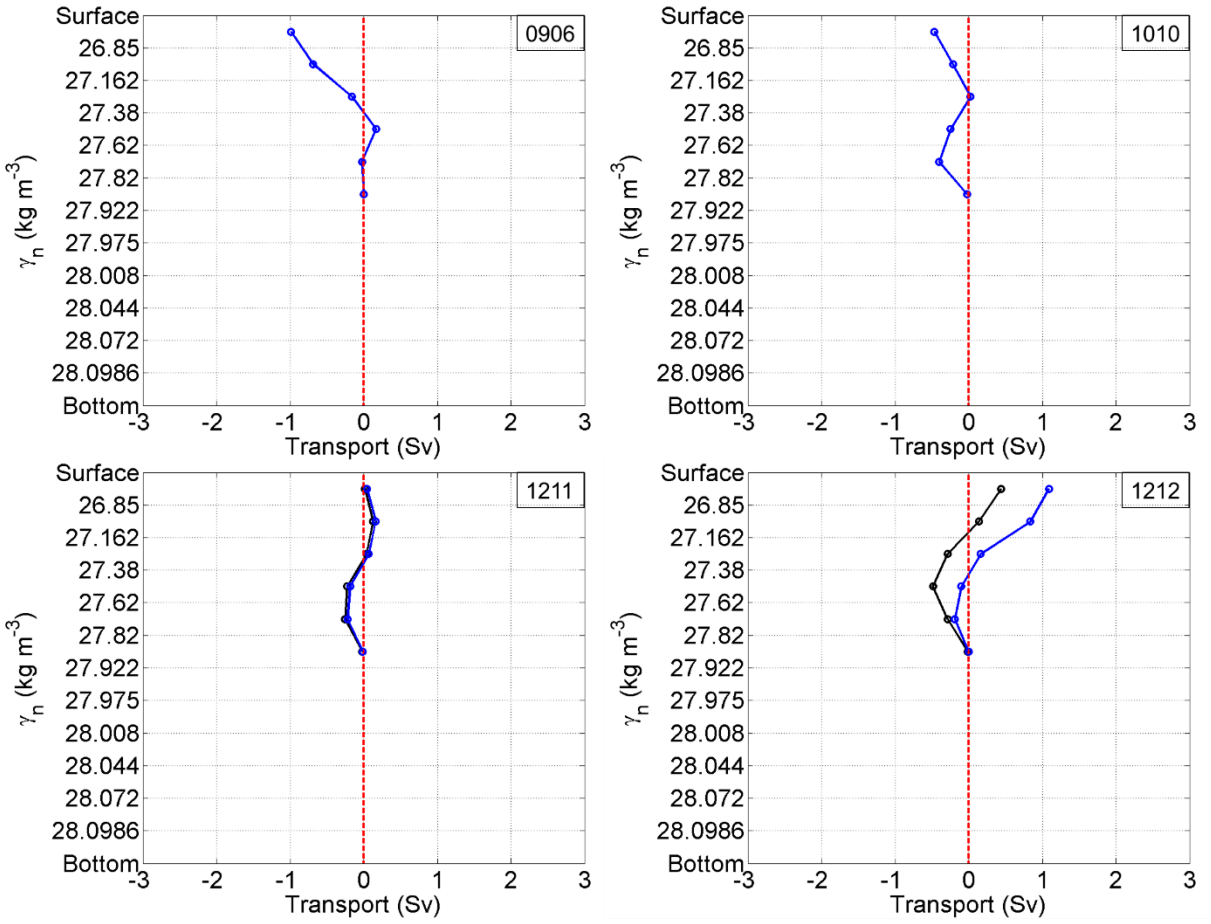

Fig. 12 – Net transport per neutral density layer in the Lanzarote Passage. RAPROCAN cruise period can be identified in the top right corner of each graph. Available LADCP adjusted transport is also plotted for the respective cruises. Blue – transport without LADCP contribution; black – LADCP adjusted geostrophic transport.

First graphs of figure 12 show a main negative transport, with a slight positive transport around the layer 27.62 kg m^{-3}. We can clearly see the transition phase in October, where the intermediate transport is also negative. This results in an inversion of the CUC transport, where the surface transport flows poleward and the intermediate transport is negative. It would be very interesting to have data for January in order to check if there is also a transition phase at that time, to close the cycle of the reversal of the transport in the LP. The Canary Upwelling Current was a key point of the study of Fraile-Nuez et al. (2010) who also observed a similar behavior. Likewise, Machín & Pelegrí (2009) identified the inversion of transport in the Lanzarote Passage as a typical feature in early fall, after the strong summer trade winds have ceased. The southward flow becomes unstable and the current suffers a westward displacement. In order to keep water mass balance, the subsurface poleward current arises and the inversion of December takes place. 1010 seems to capture the period when the current becomes unstable since we cannot see the normal northward AAIW flowing waters.

After defining 27.975 kg m^{-3} as the new layer of no motion from stations 6 to 18, we re-computed the net transport per neutral density layers and per station pairs, which will be showed in the following two pictures. To the resemblance of the last shown figure, this following one also shows a black dotted line with the net transport after applying the LADCP adjustment.

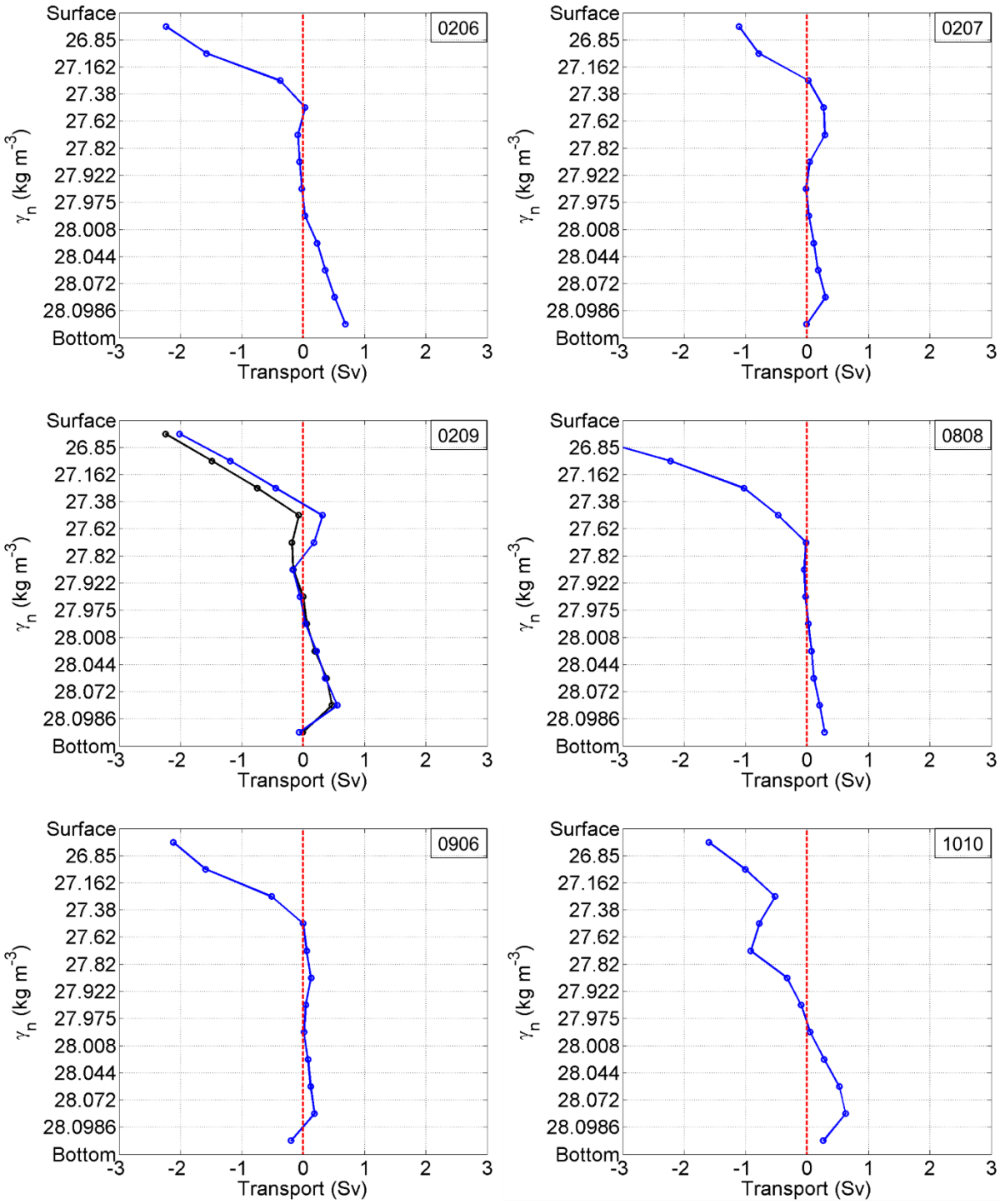
0206
0207
0209
0808
0906
1010
Surface
26.85
27.162
27.38
27.62
27.82
27.922
27.975
28.008
28.044
28.072
28.0986
Bottom
γ_n (kg m^{-3})
-3
-2
-1
0
1
2
3
Transport (Sv)

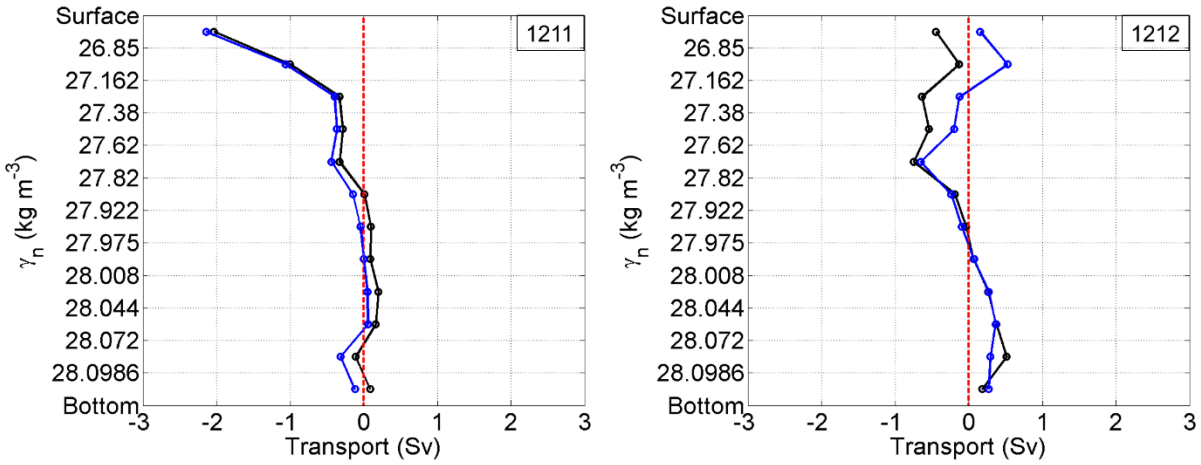

Fig. 13 – Net Transport per neutral density layer. RAPROCAN cruise period can be identified in the top right corner of each graph. Available LADCP adjusted transport is also plotted for the respective cruises. Blue – transport without LADCP contribution; black – LADCP adjusted geostrophic transport.

From figure 13 we can take much information about the transport. For instance, only in the upper layer can transport reach values over 2 Sv. Moreover, we find that when transport is very small, the sign seems to be somewhat unclear, what we can see by comparing the transport with and without the LADCP data in 1212. Please note that the 1211 graph shows the best agreement between transport derived with and without LADCP, but this is not realistic, as can be seen by the lack of stations with reference velocities in figure 9. As for 0209 and 1212, the overall difference between the two profiles is of the same order of the accumulated error of the transport. For that reason we can safely say that, for the upper layers, the transport with LADCP data is comparable to the one computed only with geostrophic velocities. Nevertheless, the LADCP is an important tool to assess a correct layer of no motion.

Next we will display the accumulated adjusted geostrophic transport per station pair. Since the dynamics of the Lanzarote Passage are not the same as for the rest of the transect, we divided the transport into thermocline and intermediated flow only in the Lanzarote Passage. For the remainder of the stations, the amounts of upper grouped layers - which compose the transport of the orange line - vary from cruise to cruise according to the direction of the flow, not the water mass type.

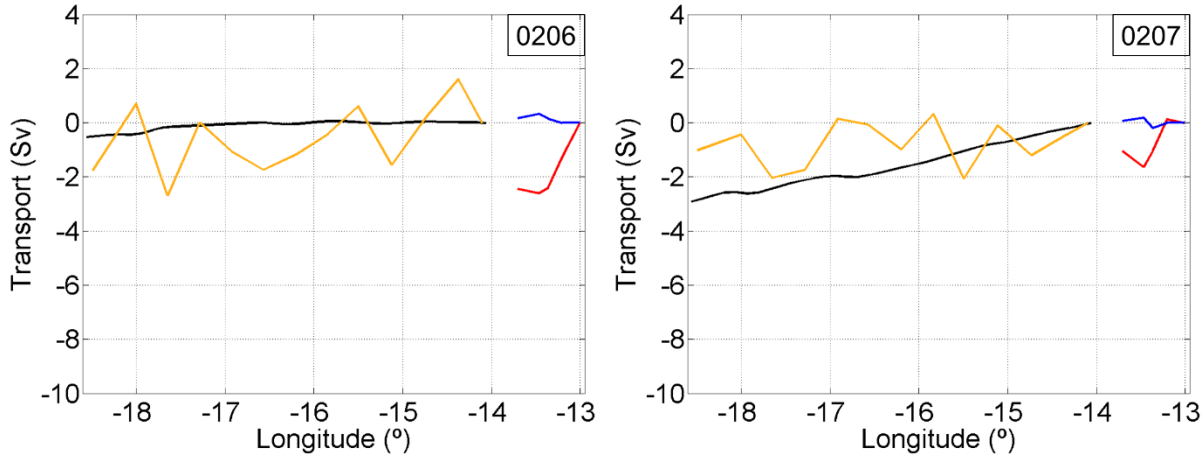

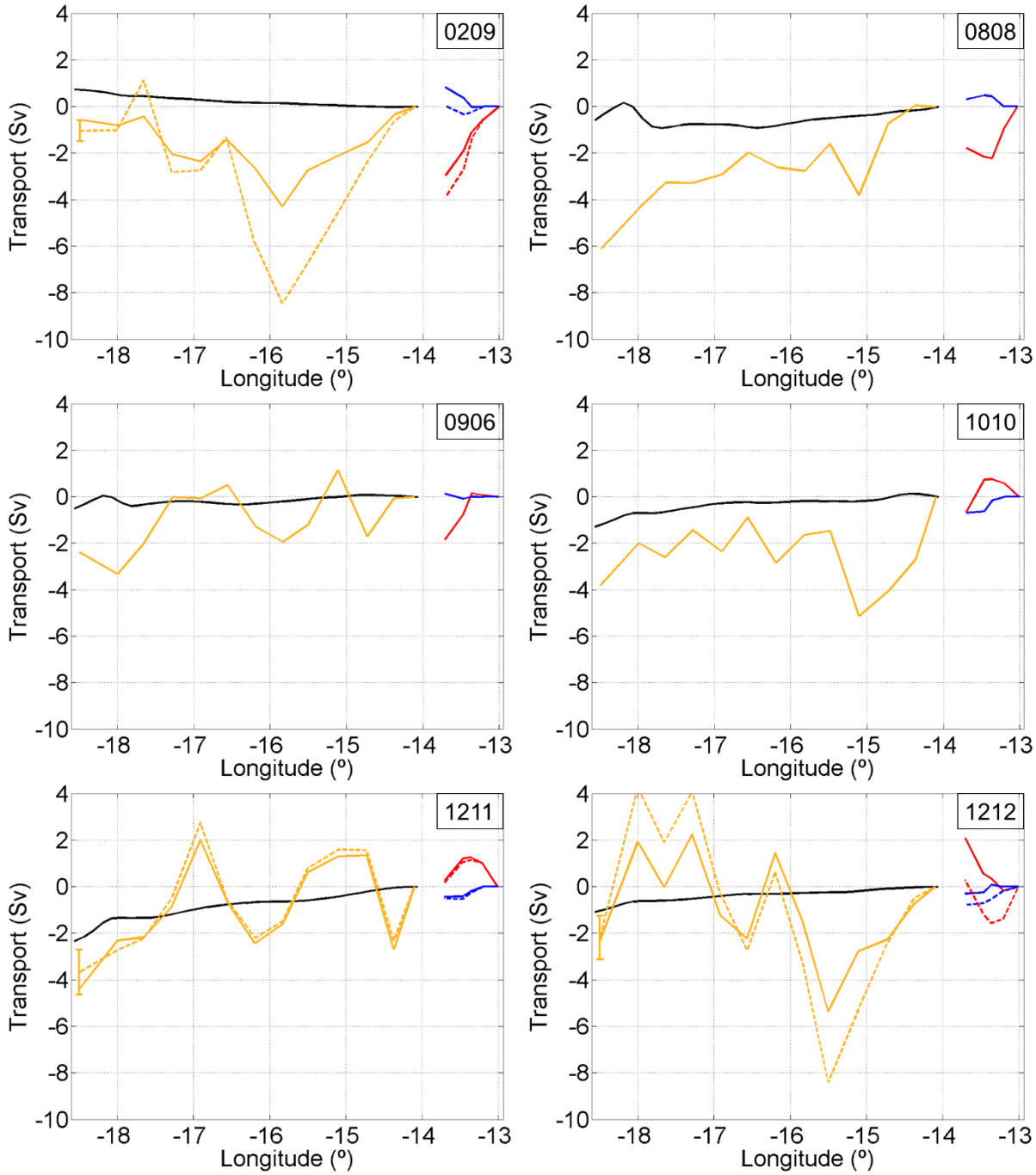

Fig. 14 – Accumulated transport per station pair. RAPROCAN cruise period can be identified in the top right corner of each graph. Red - thermocline transport; blue - intermediate waters' transport; orange - transport of net southward flowing water, with number of summed layers according to figure 13; black - Sverdrup transport. Error bars are the same as figure 11.

The saw-like curve is an indicator of the eddy presence, due to the effect of the Canary Islands in the water motion. Consequently, if we ignore these effects, we see that in many RAPROCAN cruises there is no overall slope of the transport. The exceptions are: August, where we can clearly see the Canary Current carrying water southward due to the strong negative gradient of the orange curve; and October where there is an abrupt drop of the orange curve right after the Lanzarote gap. The Meddy of 1010 is even now visible, right after the Lanzarote Gap, characterized by a local southward transport peak and a characteristic anticyclonic rotation. At all the other cruise periods, there is little accumulated transport, probably due to the westward migration of the main branch of the CC, as explained in Pérez-Hernández et al. (2013).

Notice how the black line, the Sverdrup transport, usually follows the upper layer's transport of the CC. The exception is 0209, with a very unusual, positive Sverdrup transport. For all the other cruises, the Sverdrup transport seems at the very least to explain the tendency of the accumulated transport, in accordance to Fraile-Nuez & Hernández-Guerra (2006). The uncertainty of the adjusted geostrophic transport helps to explain the Sverdrup transport, especially if we ignore the effect of the eddy-related peaks.

Pelegrí et al. (2005) found that it is actually the wind stress that dictates the CUC flow regime which is composed of NACW. As for intermediate waters, its motions are imposed by a totally different source, according to Machín & Pelegrí (2009). They found that the stretching and shrinking of the AAIW stratum in the North Atlantic tropical region induces a northward and southward motion of AAIW, respectively, in order to conserve potential vorticity. The AAIW flow reaches up to Cape Ghir, north of the Canarian Archipelago.

From figure 14, in the LP, we can see how the accumulated transport is usually zero or positive, except in October and December where there is an inversion of the flow direction. This seems to confirm the findings of Machín & Pelegrí (2009), as was already described above regarding the transport per layer in figures 6 and 12.

5. Discussion

Let us focus now on the Sverdrup transport and the respective wind stress curl. Table 4 has the same structure of table 3, featuring the results for the Sverdrup transport of the Canary Basin. From this table we can tell that the strength of this transport doesn't follow a clear seasonal pattern, for the greatest values are concerning very different periods.

Table 4 – Accumulated Sverdrup transport from 14º W to 18.5º W, for each RAPROCAN cruise period. Units in Sv.

0206	0207	0209	0808	0906	1010	1211	1212	Mean
-0.5	-2.9	0.7	-0.6	-0.5	-1.3	-2.3	-1.1	-1.1

Atkinson et al. (2010) conducted a study at 26º N of latitude where they determined the Sverdrup transport seasonality. Their results showed an intensification of the Sverdrup transport at the EBC during winter followed by a weaker than average transport until late summer where it becomes again intensified. The summer intensification can only be identified if we consider the accumulated Sverdrup transport further seaward. This showcases the difficulty in deriving the Sverdrup transport around an archipelago, for the geography interferes with the passing trade winds, creating a complex structure of alternating positive and negative wind stress curl cells, as can be seen next in figure 15.

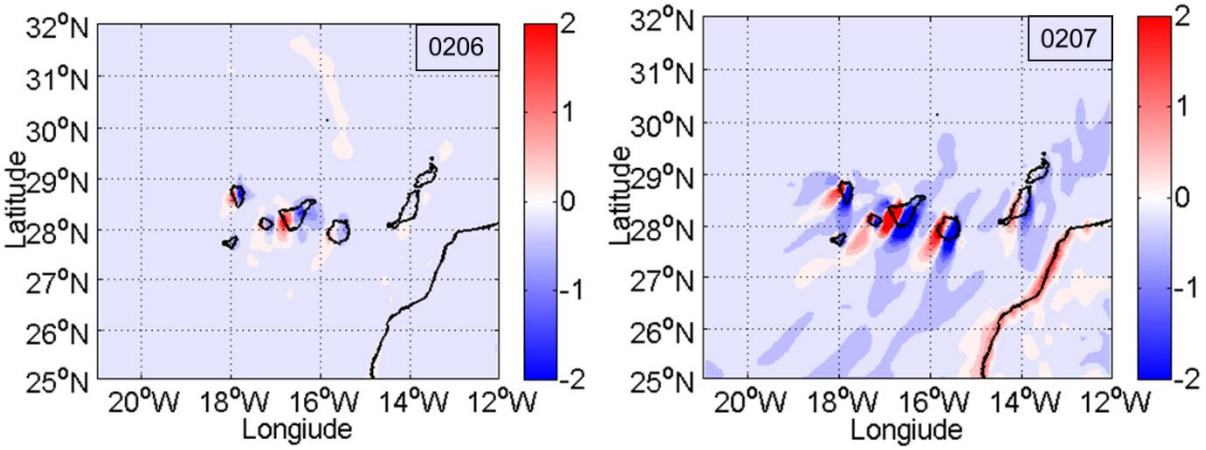

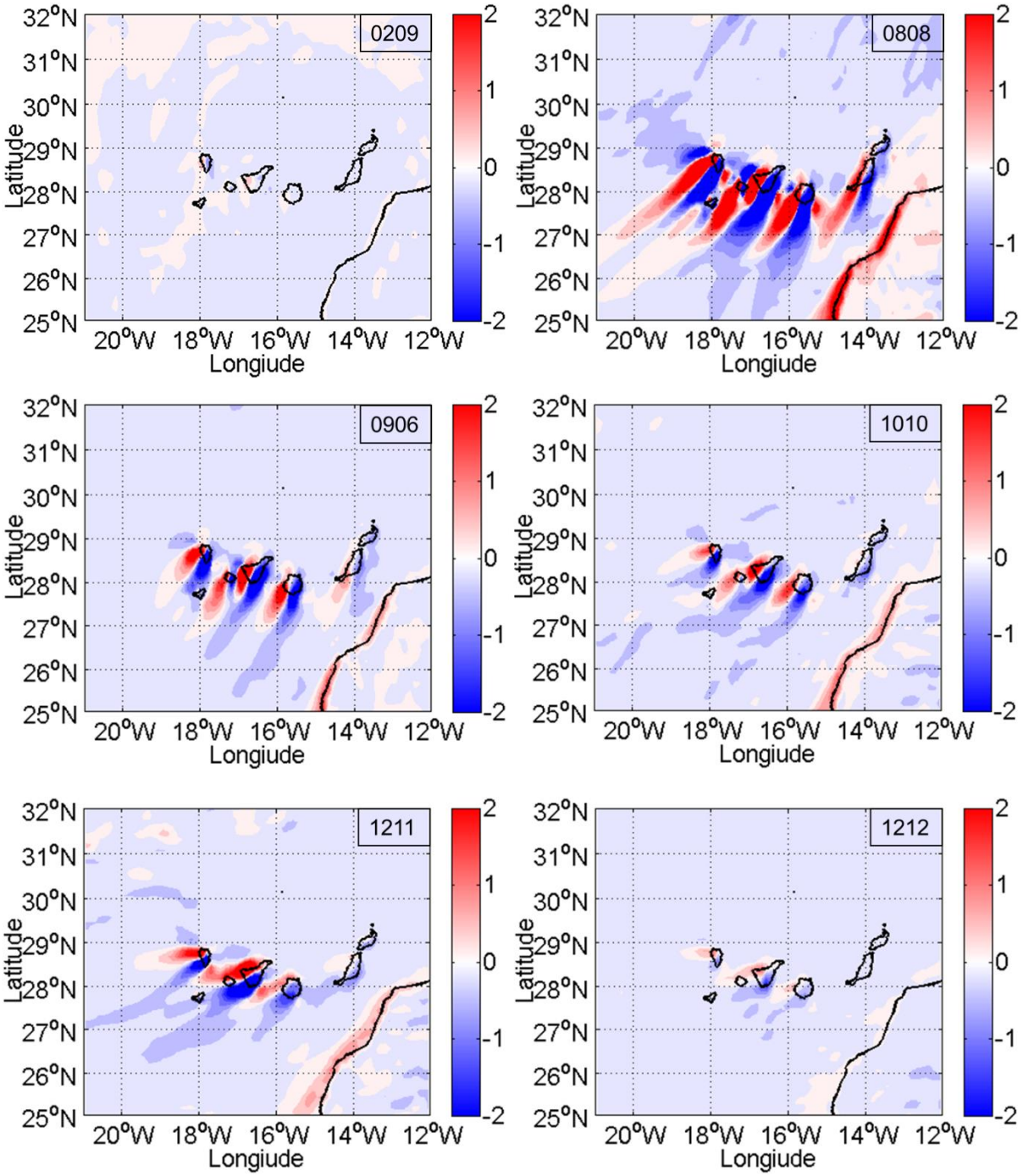

Fig. 15 – Wind stress curl of the Canary Basin. RAPROCAN cruise period can be identified in the top right corner of each graph. Bold contours for coastlines. Color-bar values in 10^{-6} N m^{-3}.

Please examine the cyclonic and anticyclonic eddies downstream of the islands. The strongest eddies are caused by the height and shape of Tenerife. This can be observed more or less with the same pattern in all cruises except 0209. Thus, we have an unusual resultant Sverdrup transport, which does not agree with the observed water transport. We must not forget that we only considered the mean wind over the RAPROCAN cruise periods, which never comprise more than 11 days. In this sense, the wind stress curl fields of figure 15 could have captured a passing mesoscale feature, such as a low pressure system, that disturbed the typical wind field (Atkinson et al., 2010).

Canary Current variability is directly linked to the local wind field and consequently to its trade wind variability, as well as the intensification or shifting of the ITCZ and the Azores High

Pressure System (Ahrens, 2009). Although this is the major forcing that controls the CC dynamics it does not fully describe them (Pedlosky, 1996). The Sverdrup theory was developed for the ocean interior, it neglects friction and vertical motion (Marshall & Plumb, 2008) and is therefore not the best fit for the EBC (Pedlosky, 1996). The Munk Solution and other circulation models may explain our results better. This requires a more detailed study which is not the aim of this study.

5.1 Temporal Variability

Trade winds depend on the position and intensity of the Azores High (H) and the Low pressure systems (L) of the doldrums (which approximately coincide with the ITCZ positioning). This circulation system, the Hadley Cell, is characterized by ascending air at equator and descending at horse latitudes. In between these latitudes are very strong winds, called easterlies or trade winds, since H rotates anti-cyclonically and therefore drives winds in the mentioned direction (Ahrens, 2009). In January, trade winds are centered between 25º-10º N and migrate to 32º-20º N in high summer (Hernández-Guerra & Nykjaer, 1997). This means that they are more or less constant in the 20º-25º N belt (Hernández-Guerra et al., 2002). The Canary Archipelago is spread around 28.5º N, so at these latitudes, the trade winds are most intense in summer and weaken in September (Fraile-Nuez et al., 2010) (Hernández-Guerra et al., 2005).

Let us now analyze the net transport of the months with the same behavior or characteristics, according to the graphs in figure 14. Table 5 summarizes and clusters water volume of the CC and CUC, Ekman and Sverdrup transports as described in section 3. All transports are subdivided into the main branch and the LP area. The last row of the table gives us a mean value for each kind of transport and each of the areas of interest.

Fall and December have very similar geostrophic accumulated transport but completely different values for the Lanzarote Passage. The CUC transport does not suffer much change from August to fall, as opposed to the total transport which decreases considerably. Justifying these bearings by comparison with the local Ekman and Sverdrup transports' is very difficult. The LP Sverdrup transport, as well as the LP Ekman transport, is approximately constant throughout the year. The latter has a small maximum in August, whereas for the rest of the transect it is strongest in December. We must keep in mind that these values are obtained from transports only up to 18.5º W and will therefore not show any resemblance between the Sverdrup transport and the Canary Current if the CC has moved westward. This could explain why Sverdrup and water transports do not behave alike. The total Ekman transport contributes only little to the geostrophic transport and is therefore not of major importance.

Table 5 – Mean accumulated transport per month or season, for the LP only and the remainder of the transect. For periods with LADCP data, a mean value was taken from the initial and the adjusted transport. Units in Sv.

	Water Volume		Sverdrup		Ekman	
	CC	CUC	Rest	LP	Rest	LP
February	-1.10	-2.58	-0.90	-0.40	0.01	0.00
August	-6.10	-1.80	-0.60	-0.60	0.27	0.03
Fall	-3.10	-1.25	-0.90	-0.45	0.10	0.02
December	-3.15	0.73	-1.70	-0.45	0.19	0.03
Mean	-3.36	-1.23	-1.03	-0.48	0.14	0.02

Given the importance of the Atlantic Meridional Overturning Circulation and the UMO to our understanding of the climate variability, we now present the results of the monthly averaged UMO variability in comparison to the obtained adjusted geostrophic transport. Chidichimo et al. (2010) studied the relationship between the Atlantic MOC and the EBC, while Pérez-Hernández et al. (in prep.) discovered a high correlation between the under mid-ocean (UMO)

current variability and the CUC transport. To discuss this, we present a graphic with the results for the standardized, adjusted, accumulated geostrophic transport from our RAPROCAN cruises (numbered), as well as standardized CUC transport from scientific articles (blue), and compared it to the standardized UMO curve and its monthly standard deviation (figure 16). The numbered data points present different colors depending on the amount of layers considered as the CUC transport (orange and red). In the case of the green data points, the main branch of the Canary Current was considered for the sake of completeness of this analysis.

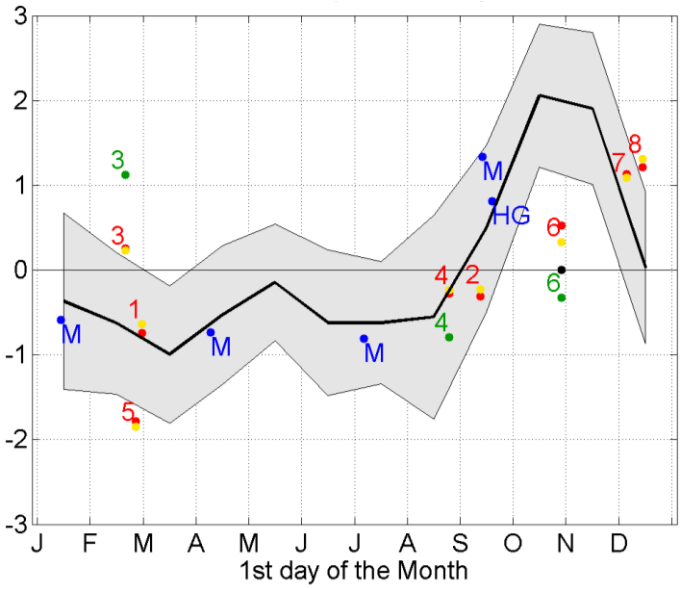

Fig. 16 – Normalized transport variability compared to the normalized monthly upper mid-ocean transport. Black – UMO with respective shaded monthly standard deviation in grey; red – accumulated thermocline transport of CUC; orange – Accumulated transport in LP for upper layers with same direction of flow; green – main branch of the Canary Current's transport; blue – CUC thermocline transport from literature, where M stands for Machín et al. (2006) and HG stands for Hernández-Guerra et al. (2005). Numbers refer to cruises as listed in table 1.

The figure shows that the Canary Upwelling Current is closest to the UMO variability. The difference between the thermocline transport and the one we obtained by limiting the transport to only the top 2 or 3 layers - which flow in the same direction and vary broadly from cruise to cruise - is not striking. Furthermore, by considering what we identified as the main branch of the CC in our results, its normalized transport seems to be less related to the UMO curve. Also, note how the CUC transport obtained through inverse models in Machín et al. (2006) and in Hernández-Guerra et al. (2005) seems to explain quite accurately the UMO variability.

We can see that there is a high interannual variability in February. Since the wind field was very different from cruise to cruise in this month, we assume that this variability is normal for this month, due to the passing storms that are so typical at this time of the year, in this region.

The transport obtained in the cruise at the end of October is another matter. Taking a closer look at the figure we can distinguish a black dot in the end of October. This is the normalized UMO transport for the same period as the RAPROCAN cruise 1010. Through it, we can explain why our results are so different from the UMO curve: the upper mid-ocean transport was very weak at that time. All the other CUC transports depicted here seem to be in good agreement with the UMO variability.

6. Conclusion

This study processes the data of 8 different RAPROCAN cruises in order to obtain the volume transport of the Canary Current as accurate as possible. This includes the dynamics of the Canary Upwelling Current, located in a small section between the Lanzarote Island and the

Moroccan coast, known as the Lanzarote Passage. For this purpose, we analyze data from CTD casts, and in some cruises also LADCP casts, for the individual period of each cruise. Since data covers different months, we hoped to recognize a pattern in the seasonal variability of the CC and the CUC, separately. To check into what extend the local wind stress curl regulated the flow of the currents we computed the Sverdrup transport for comparison to the water transport.

The LP current is not dominated by the local wind stress curl, supporting the study of Machín & Pelegrí (2009). Sverdrup transport seems to describe the tendency of the adjusted, accumulated geostrophic transport of the main branch of the Canary Current, for all cruises except for February 2009. Further investigation is needed to justify this unexpected behavior. We found that caution is needed in the computation of the Sverdrup transport due to its sensitivity to small changes in the selection of the grid points of the wind stress curl field. The wind stress curl field, for the different cruises, indicates an enormous spatial variability, where the only approximately permanent features are the positive and negative vortexes south to southwest of the islands.

The Lanzarote Passage's local dynamic was identified, featuring a seasonal inversion of intermediate water's flow, just as was identified in Machín & Pelegrí (2009), Hernández-Guerra et al. (2003) and Fraile-Nuez et al. (2010), but with a shift in the period when it occurs. CUC transport varies throughout the RAPROCAN cruises approximately between [-3.9; 0.3] Sv. The thermocline and intermediate waters from station 6 to 18 exhibited a transport which fluctuates between [-6.1; -1] Sv, with the strongest transport taking place in August and the weakest in February 2007. This agrees approximately with the results of Fraile-Nuez et al. (2010), Hernández-Guerra et al. (2003) and Comas-Rodríguez (2011).

Results confirm the existence of a relationship between the monthly variability of the thermocline current of the LP – the Canary Upwelling Current - and the UMO current variability, directly related to the Atlantic Meridional Overturning Circulation. The special case of October 2010, when the mean UMO transport is most distant to the CUC transport, is a period where the UMO itself is much lower than usually. This highlights the robustness of the correlation between the upper mid-ocean variability and the Canary Upwelling Current variability.

In sum, more cruises covering different months should be carried out. The fall and winter months are of special interest regarding the Lanzarote Passage flow. In the future, we will have enough data to understand the whole Canary Current temporal and spatial variability. This will allow us to comprehend the Meridional Overturning Circulation's variability and increase our knowledge of its impact on our climate.

Appendix A - LADCP bottom-tracking review

In this appendix we take a closer look on the characteristics of LADCP data, through a separate RAPROCAN dataset of 53 stations of October 2013. The purpose of this separate study is to clarify which types of LADCP data retrieval are more alike and which ones are more reliable.

The need to better understand deep ocean dynamics encouraged the development of new velocity profiling instruments. In this sense, LADCP came as a welcome innovation, giving a direct insight on ocean bottom velocities, with more spatial flexibility, as well as reduced maintenance time and costs (Fischer & Visbeck, 1993). This technology, although reliable, still has some limitations and disadvantages, mainly due to noise related uncertainties and a complicated data processing software (Visbeck, 2002; Deines, 1999; Thurnherr, 2011).

The LADCP measures velocities based on the Doppler Effect by emitting four beams of acoustic signals and receiving the corresponding echo from suspended particles in the water column (Deines, 1999). Each beam measures independently a velocity component from a set of 3 orthogonal velocities, the extra beam is used for redundancy and error calculations. These measured velocities need to be adjusted to absolute velocities by adding constraints to the processed LADCP (Thurnherr, 2011), (Visbeck, 2002). The constraint applied to our data was the so-called bottom-tracking (BT), where the velocity difference between the LADCP profiler and the bottom of the water column is used. This allows us to correct the LADCP measured current velocities by including the movement of the LADCP itself, which is lowered with the rosette. The velocities obtained through this will be used for geostrophic velocity corrections.

There is more than one way to acquire the bottom tracking (Visbeck, 2002). We will only mention two types, the intrinsic BT of the LADCP instrument manufacturer – RDIBT - and the post-processed BT, calculated by Visbecks software, here called ownBT. Together with the different LADCP measuring units we arrive at four different processed data combinations: without the BT (noBT), RDIBT with LADCP from only the master unit looking down (onlydownBT), BT applied through Visbeck's software to the whole WH unit (ownBT) and RDIBT applied to the whole WH unit (RDIBT). Other works, such as Thurnherr (2003), already determined that RDIBT has a better range resolution than the ownBT and is therefore considered to retrieve the most reliable data. Therefore, and as was done by Comas-Rodríguez et al. (2010), we used that intrinsic bottom track data of the instrument to assess the quality of the 3 other methods.

To accomplish this, we chose two different approaches. One of them was to calculate the velocity difference between two methods for each station, for each depth, of each velocity component. The methods closest to RDIBT, and consequently the best methods, would have the smallest velocity differences. We then conducted a series of statistics tests, presented in the subsection entitled Error bars. The other approach was to calculate the correlation coefficient for each station, of each velocity component. The results for this are presented in the next subsection.

Correlations

To calculate the correlation coefficient we first standardized the velocity values where $\vec{v} = (u, v)$ and each component is an i (vertical) by j (horizontal) matrix of i=421 and j=53.

$$\vec{v}(standardized)_{i,j} = \frac{\left(\vec{v}_{i,j} - \mu(\vec{v})_j\right)}{\sigma(\vec{v})_j} \tag{14}$$

μ is the mean velocity along the water column and σ is the respective standard deviation. We then made sure that the standardized velocities had zero mean and standard deviation of 1. This is a necessary condition to obtain correlation coefficients through the covariance operation (Jolliffe, 2002).

Table 6 summarizes the correlations computed between all methods and for both horizontal velocity components. It shows minima, maxima, mean values and also the standard deviations. The values are all over 90%, except for correlations with onlydownBT. The best results are those of ownBT. This means that onlydownBT profiles' vertical variations are more distant to the other methods. It becomes clear that, regardless of the method, the zonal velocity has always more problematic stations than the meridional velocity. The methods seem to be independent from one another since the best and the worst correlated stations of one method are never the same for the other methods. It also excludes the possibility of the correlation values being biased by one particular station.

Table 6 - Correlations between RDIBT and the other methods. The respective station numbers are also listed.

	noBT		onlydownBT		ownBT	
	u	v	u	v	u	v
Minimum correlation	0.91	0.93	0.58	0.60	0.96	0.97
Station number	20;	21;	22;	51;	19;	20;
Maximum correlation	1.00	1.00	0.99	0.99	1.00	1.00
Station number	46; 52;	49;	2;	3;	1; 26; 53;	38; 51;
Mean correlation	0.98	0.99	0.91	0.92	0.99	1.00
Standard deviation	0.02	0.01	0.08	0.08	0.01	0.01

Error bars

After computing the difference for the velocities between each two methods, 3 graphs were plotted, showing the mean difference and the standard deviation error bars, for every station, for each velocity component. A simple standard deviation threshold of 0.01 m/s was defined in order do have a common comparison ground for the three methods. Looking at the figures it becomes very clear that onlydownBT has the most different profiles, with very large error bars, whereas ownBT showed the best results. This is in agreement to the correlations computed in the previous subsection.

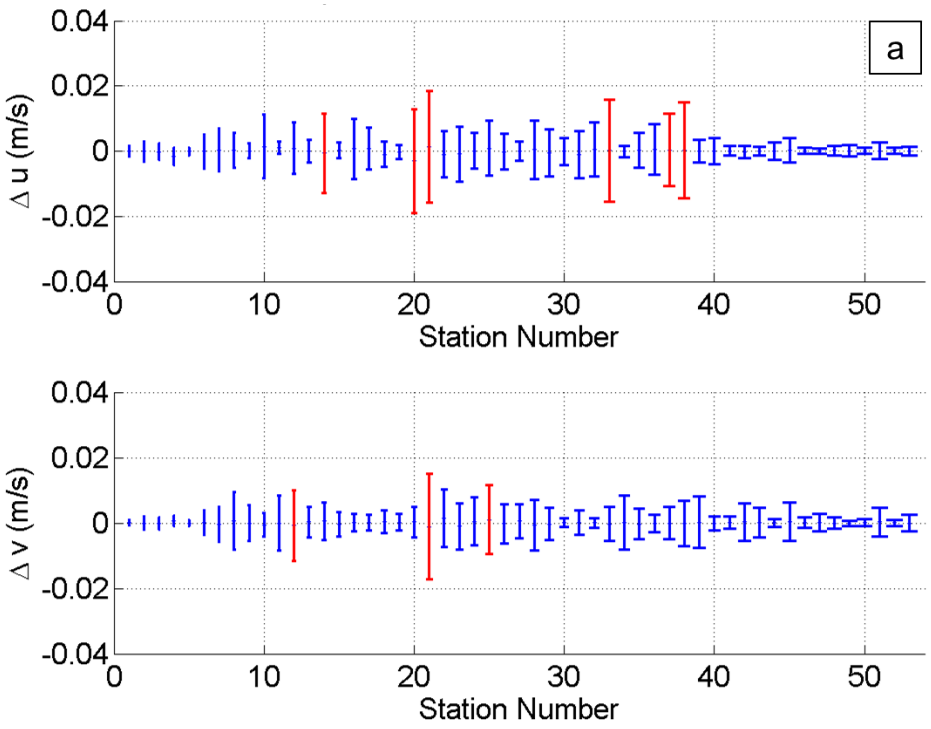

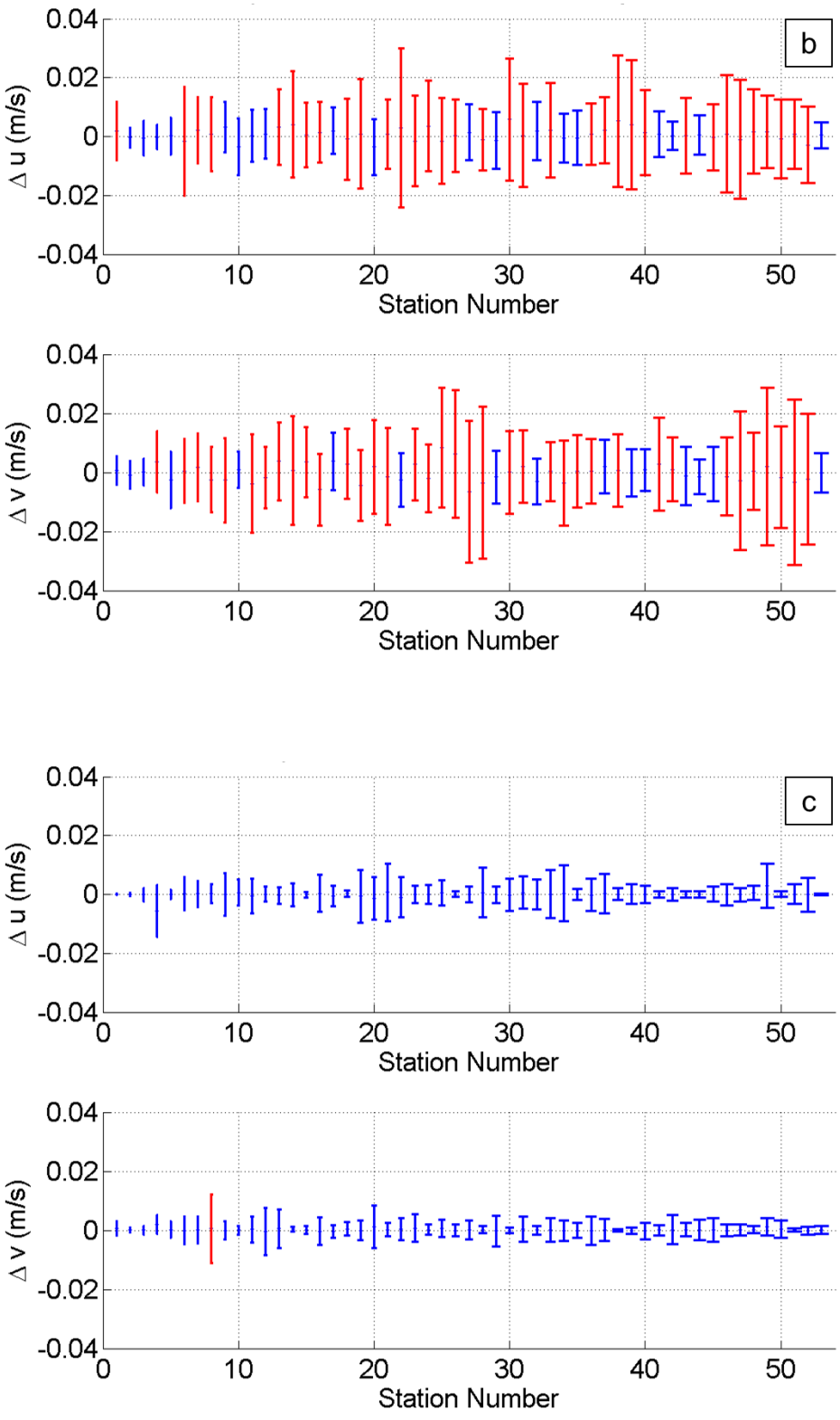

Fig. 17 – Top (a): RDIBT-noBT error bars; center (b): RDIBT-onlydownBT error bars; bottom (c): RDIBT-ownBT error bars. In red are the stations whose standard deviations overcame the chosen threshold.

We then removed the top ten velocity entries from the profile and calculated the same error bars (not shown). This process was repeated for every method comparison, and subsequently the bottom ten velocity entries were removed and the process was repeated. The results for noBT and for onlydownBT improved by removing the top ten velocities from the profile, showing that the worst correspondence is at the top of the profile. The difference is striking in onlydownBT error bars. There was no important alteration in the ownBT results. This comes to show one of the weak points of BT LADCP data, namely, that it strongly depends on its ability to pinpoint the bottom, without noise interference, such as vessel machinery and contamination of previous pings or even the amount of suspended matter in the deep ocean (which influences the scattering of the acoustic signal) (Deines, 1999).

We conclude that ownBT is the closest method to RDIBT, closely followed by noBT. OnlydownBT presents the most substantial differences, especially at the top of the profile.

7. References

Book

Ahrens, C. D. (2009). *Meteorology Today: An Introduction to Weather, Climate, and the Environment* (Ninth Edition), Brooks/Cole, Cengage Learning.

Apel, J. R. (1999). *Principles of ocean physics – International geophysics series* (Fifth edition). Academic Press.

Jolliffe, I. T. (2002). *Principal Component Analysis* (Second Edition), Springer.

Marshall, J., and R. A. Plumb (2008). *Atmosphere, ocean, and climate dynamics: an introductory text – International geophysics series*; v. 93. Elsevier Academic Press.

Pedlosky, J. (1996). *Ocean Circulation Theory* (First Edition), Springer.

Protter, M. H., P.E. Protter (1988). *Calculus with Analytic Geometry* (Fourth edition), Jones & Bartlett Learning.

Scientific Article

Aaboe, S., O. A. Nøst, and E. Hansen (2009). Along-slope variability of barotropic transport in the Nordic Seas: Simplified dynamics tested against observations, *J. Geophys. Res.*, 114, C03009, doi:10.1029/2008JC005094.

Atkinson, C. P., Bryden, H. L., Hirschi, J., & Kanzow, T. (2010). On the seasonal cycles and variability of Florida Straits, Ekman and Sverdrup transports at 26 N in the Atlantic Ocean. *Ocean Science*, 6(4), 837-859.

Chidichimo, M. P., Kanzow, T., Cunningham, S. A., Johns, W. E., & Marotzke, J. (2010). The contribution of eastern-boundary density variations to the Atlantic meridional overturning circulation at 26.5 N. *Ocean Science*, 6(2), 475-490.

Comas-Rodríguez, I., A. Hernández-Guerra, and E. McDonagh (2010). Referencing geostrophic velocities using ADCP data at 24.5°N (North Atlantic), *Sci. Mar.*, 74(2), 331–338, doi:10.3989/scimar.2010.74n2331.

Cunningham, S. A., Kanzow, T., Rayner, D., Baringer, M. O., Johns, W. E., Marotzke, J., ... & Bryden, H. L. (2007). Temporal variability of the Atlantic meridional overturning circulation at 26.5º N. *Science*, 317(5840), 935-938.

Egbert, G. D., & Erofeeva, S. Y. (2002). Efficient inverse modeling of barotropic ocean tides. *Journal of Atmospheric and Oceanic Technology*, 19(2), 183-204.

Fischer, J. and M. Visbeck (1993). Deep Velocity Profiling with Self-contained ADCPs, *Journal of Atmospheric and Oceanic Technology*, 10 (5). pp. 764-773. DOI 10.1175/1520-0426(1993)

Fraile-Nuez, E., and A. Hernández-Guerra (2006), Wind-driven circulation for the eastern North Atlantic subtropical gyre from argo data, *Geophys. Res. Lett.*, 33, L03601, doi:10.1029/2005GL025122.

Fraile-Nuez, E., F. Machín, P. Vélez-Belchí, F. López-Laatzen, R. Borges, V. Benítez-Barrios, and A. Hernández-Guerra (2010). Nine years of mass transport data in the eastern boundary of the North Atlantic Subtropical Gyre, *J. Geophys. Res.*, 115, C09009, doi:10.1029/2010JC006161.

Hernández-Guerra, A., & Nykjaer, L. (1997). Sea surface temperature variability off north-west Africa: 1981-1989. *International Journal of Remote Sensing*, 18(12), 2539-2558.

Hernández-Guerra, A., F. Machín, A. Antoranz, J. Cisneros-Aguirre, C. Gordo, A. Marrero-Díaz, A. Martínez, A.W. Ratsimandresey, A. Rodríguez-Santana, P. Sangrá, F. López-Laazen, G. Parrilla, J.L. Pelegrí (2002). Temporal variability of mass transport in the Canary Current, *Deep Sea Res. Part II : Top. Stud. Oceanogr.*, 49(17), 3415–3426.

Hernández-Guerra, A., Fraile-Nuez, E., Borges, R., López-Laatzen, F., Vélez-Belchí, P., Parrilla, G., & Müller, T. J. (2003). Transport variability in the Lanzarote passage (eastern boundary current of the North Atlantic subtropical Gyre). *Deep Sea Research Part I: Oceanographic Research Papers*, 50(2), 189-200.

Hernández-Guerra, A., E. Fraile-Nuez, F. López-Laatzen, A. Martínez, G. Parrilla, and P. Vélez-Belchí (2005). Canary Current and North Equatorial Current from an inverse box model, *J. Geophys. Res.*, 110, C12019, doi:10.1029/2005JC003032.

Jackett, D., T. J. McDougall (1997). A Neutral Density Variable for the World's Oceans, *Journal of Physical Oceanography*, Volume 27, Issue 2 (February 1997) pp. 237-263.

Köhl, A., & Stammer, D. (2008). Variability of the meridional overturning in the North Atlantic from the 50-year GECCO state estimation. *Journal of Physical Oceanography*, 38(9), 1913-1930.

Machín, F., A. Hernández-Guerra, and J. Pelegrí (2006). Mass fluxes in the Canary Basin, *Prog. Oceanogr.*, 70(2–4), 416–447.

Machín, F., & Pelegrí, J. L. (2009). Northward penetration of Antarctic intermediate water off Northwest Africa. *Journal of Physical Oceanography*, 39(3), 512-535.

Machín, F., Pelegrí, J. L., Fraile-Nuez, E., Vélez-Belchí, P., López-Laatzen, F., & Hernández-Guerra, A. (2010). Seasonal flow reversals of Intermediate Waters in the Canary Current System east of the Canary Islands. *Journal of Physical Oceanography*, 40(8), 1902-1909.

Matei, D., Baehr, J., Jungclaus, J. H., Haak, H., Müller, W. A., & Marotzke, J. (2012). Multiyear prediction of monthly mean Atlantic meridional overturning circulation at 26.5º N. *Science*, 335(6064), 76-79.

McCarthy, G., Frajka-Williams, E., Johns, W. E., Baringer, M. O., Meinen, C. S., Bryden, H. L., ... & Cunningham, S. A. (2012). Observed interannual variability of the Atlantic meridional overturning circulation at 26.5º N. *Geophysical Research Letters*, 39(19).

Pacheco, M. M. & A. Hernandez-Guerra (1999). Seasonal variability of recurrent phytoplankton pigment patterns in the Canary Islands area, *International Journal of Remote Sensing*, 20:7, 1405-1418, DOI:10.1080/014311699212795

Pelegrí, J. L., Arístegui, J., Cana, L., González-Dávila, M., Hernández-Guerra, A., Hernández-León, S., ... & Santana-Casiano, M. (2005). Coupling between the open ocean and the coastal upwelling region off northwest Africa: water recirculation and offshore pumping of organic matter. *Journal of Marine Systems*, 54(1), 3-37.

Pelegrí, J. L., Marrero-Díaz, A., & Ratsimandresey, A. W. (2006). Nutrient irrigation of the North Atlantic. *Progress in Oceanography*, 70(2), 366-406.

Pérez-Hernández, D. M., A. Hernández-Guerra, E. Fraile-Nuez, I. Comas-Rodríguez, V. M. Benítez-Barrios, J. F. Domínguez-Yanes, P. Vélez-Belchí and D. De Armas (2013). The source of the Canary current in fall 2009, *J. Geophys. Res. Oceans*, 118, doi:10.1002/jgrc.20227.

Pérez-Hernández, D. M., et al. (in prep). The Canary Basin contribution to the 26º N AMOC seasonality.

Rayner, D., Hirschi, J. J. M., Kanzow, T., Johns, W. E., Wright, P. G., Frajka-Williams, E., ... & Cunningham, S. A. (2011). Monitoring the Atlantic meridional overturning circulation. *Deep Sea Research Part II: Topical Studies in Oceanography*, 58(17), 1744-1753.

Visbeck, M. (2002). Deep Velocity Profiling Using Lowered Acoustic Doppler Current Profilers: Bottom Track and Inverse Solutions. *J. Atm. & Oceanic Tech.*, 19, 794-807.

M.S. or Ph.D. Dissertation

Atkinson, C.P. (2011). *Variability of the Atlantic Meridional Overturning Circulation at 26º N*. Philosophy Doctoral's Thesis. Faculty of Natural and Environmental Sciences. School of Ocean and Earth Science – University of Southampton, Southampton. 320pp.

Comas-Rodríguez, I. (2011). *The Azores Current System and the Canary Current from CTD and ADCP data*. Oceanography Doctoral's Thesis. Facultad de Ciencias del Mar – Universidad de Las Palmas de Gran Canaria, Las Palmas de Gran Canaria. 184pp.

Mock, C.A. (2011). *Water Masses, Mass Transport and Variability of the Canary Current in autumn*. Oceanography Master's Thesis. Facultad de Ciencias del Mar – Universidad de Las Palmas de Gran Canaria, Las Palmas de Gran Canaria. 30pp.

Digital Document

Cana-Cascallar, L. (2014). *The Weather Research and Forecasting (WRF) model*. IOCAG. Tafira, Gran Canaria, Spain.

Online Document

Averaging, Errors & Uncertainty (2014). Lab Manual - Department of Physics & Astronomy, Undergraduate Labs, University of Pennsylvania. Philadelphia, USA. [Accessed 10th May 2014] at: https://www.physics.upenn.edu/uglabs/lab_manual/Error_Analysis.pdf

Bell, S. (2001). *A Beginner's Guide to Uncertainty of Measurement - Measurement Good Practice Guide No. 11* (Issue 2). National Physical Laboratory, Teddington, Middlesex, United Kingdom. [Accessed 28th May 2014] at: https://www.wmo.int/pages/prog/gcos/documents/gruanmanuals/UK_NPL/mgpg11.pdf

Dee, D. & National Center for Atmospheric Research Staff (Eds) (2013). *The Climate Data Guide: ERA-Interim*. [Accessed 22nd June 2014] at: https://climatedataguide.ucar.edu/climate-data/era-interim

Deines K.L. (1999). *Backscatter Estimation Using Broadband Acoustic Doppler Current Profilers,* Reprinted by permission of the IEEE conference San Diego, California. [Accessed 24th March 2014] at: http://www.comm-tec.com/library/technical_papers/rdi/echopaper.pdf

ECMWF (2014). ERA Project, United Kingdom. [Accessed 18th June 2014] at: http://www.ecmwf.int

MathWorks (2014) [Accessed 22th June 2014] at: http://www.mathworks.com/company/?s_cid=wiki_mathworks_5

RAPID (2014). *Rapid Climate Change (RAPID and RAPID-WATCH) - Natural Environment Research,* National Oceanography Centre Southampton, University of Miami, Rosenstiel School of Marine and Atmospheric Science, Atlantic Oceanographic and Meteorological Laboratory. [Accessed 3rd July 2014] at: http://www.bodc.ac.uk/projects/uk/rapid/

RAPROCAN (2014). *Radial Profunda de Canarias (Canary Deep Hydrographic Section) – Instituto Español de Oceanografía.* [Accessed 19th March 2014] at: http://www.oceanografia.es/raprocan/

Thurnherr, A.M. (2011). *How To Process LADCP Data With the LDEO Software,* (Version IX.7). [Accessed 24th February 2014] at: ftp://ftp.ldeo.columbia.edu/pub/ant/LADCP/UserManuals/how-to.pdf

Thurnherr, A.M. (2003). *RDI LADCP Cruise Report - Aurora Australis, Voyage 4, 2003.* [accessed 25th February 2014] at: ftp://ftp.ldeo.columbia.edu/pub/LADCP/Cruises/A0304/LADCP_CruiseReport.pdf

TOPEX (2014). *The OSU TOPEX/Poseidon Global Inverse Solution TPXO* - National Science Foundation, the Office of Naval Research and the National Aeronautics and Space Administration- [Accessed 21st April 2014] at: http://volkov.oce.orst.edu/tides/global.html

WRF (2014). *Weather Research Forecasting model* - University Corporation for Atmospheric Research (UCAR), USA. [Accessed: 5th May 2014] at: http://www.wrf-model.org/index.php